Sulphur behaviour and redox conditions in etnean magmas during magma differentiation and degassing

Emanuela Gennaro, Antonio Paonita, Giada Iacono-Marziano, Yves Moussallam, Michel Pichavant, Nial Peters, Caroline Martel

Sulphur behaviour and redox conditions in Etnean magmas during magma differentiation and degassing

Emanuela Gennaro [a*], Antonio Paonita [a], Giada Iacono-Marziano [b], Yves Moussallam [c], Michel Pichavant [b], Nial Peters [d], Caroline Martel [b]

[a] *Istituto Nazionale di Geofisica e Vulcanologia, Sezione di Palermo, Via Ugo La Malfa 153, 90146 Palermo, Italy*

[b] *Institut des Sciences de la Terre d'Orléans (ISTO) UMR 7327, Université d'Orléans - CNRS - BRGM, Campus Géosciences, 1A rue de la Férollerie, 45071 Orléans, Cedex 2 (France)*

[c] *Lamont-Doherty Earth Observatory, Columbia University, 61 Route 9W, Palisades, New York 10964-1000, USA*

[d] *Department of Geography, University of Cambridge, Downing Place,* 20 Downing Place, *Cambridge, CB2 3EN, UK*

*corresponding author: emanuelagennaro@live.it

ABSTRACT

Sulphur behaviour and variations in redox conditions during magma differentiation and degassing in Mt. Etna (Italy) volcanic system have been explored by integrating the study of olivine-hosted melt inclusions (MIs) with an experimental survey of sulphur solubility in hydrous basaltic magmas.

Sulphur solubility experiments were performed at conditions relevant to the Etnean plumbing system (1200 °C, 200 MPa and oxygen fugacity between NNO+0.2 and NNO+1.7, with NNO being the Nickel-Nickel Oxide buffer), and their results confirm the important control of oxygen fugacity (fO_2) on S abundance in mafic magmas and on S partitioning between fluid and melt phases ($DS^{fluid/melt}$). The observed $DS^{fluid/melt}$ value increases from 51±4 to 146±6 when fO_2 decreases from NNO+1.7±0.5 to NNO+0.3.

Based on the calculated $DS^{fluid/melt}$ and a careful selection of previously published data, an empirical model is proposed for basaltic magmas in order to predict the variation of $DS^{fluid/melt}$ values upon variations in P (25-300 MPa), T (1030-1200°C) and fO_2 (between NNO-0.8 and NNO+2.4).

Olivine-hosted melt inclusions (Fo_{89-91}) from tephra of the prehistoric (4 ka BP) sub-plinian picritic eruption, named FS ("*Fall Stratified*"), have been investigated for their major element compositions, volatile contents and iron speciation (expressed as $Fe^{3+}/\Sigma Fe$ ratio). These primitive MIs present S content from 235±77 to 3445±168 ppm, while oxygen fugacity values, estimated from $Fe^{3+}/\Sigma Fe$ ratios, range from NNO+0.7±0.2 to NNO+1.6±0.2.

Iron speciation has also been investigated in more evolved and volatile-poorer Etnean MIs. The only primitive melt inclusion from Mt. Spagnolo eruption (4-15 ka BP) presents a S content of 1515±49 ppm and an estimated fO_2 of NNO+1.4±0.1. The more evolved MIs (from 2002/2003, 2006, 2008/2009 and 2013 eruptions) have S content lower than 500 ppm, and their $Fe^{3+}/\Sigma Fe$ ratios result in fO_2 between NNO-0.9±0.1 and NNO+0.4±0.1.

Redox conditions and S behaviour in Etnean magmas during degassing and fractional crystallization were modelled coupling MELTS code with our empirical $DS^{fluid/melt}$ model. Starting from a FS-type magma composition and upon decrease of T and P, fractional crystallization of olivine, clinopyroxene, spinel and plagioclase causes a significant fO_2 decrease. The fO_2 reduction, in turn, causes a decrease in sulphur solubility and an increase in $DS^{fluid/melt}$, promoting S exsolution during magma ascent, which further enhances the reduction of fO_2. For the evolved melt inclusions of 2002-2013 eruptions, magma differentiation may therefore have played a crucial role in decreasing redox conditions and favouring efficient S degassing.

Differently, during the unusual FS eruption, only limited melt evolution is observed and S exsolution seems to have been triggered by a major pressure decrease accompanied by H_2O and CO_2 exsolution during fast magmatic ascent.

Keywords: melt inclusions; Mt. Etna; redox conditions; sulphur solubility experiments; XANES $Fe^{3+}/\Sigma Fe$.

INTRODUCTION

Volatile components play a key role in volcanic systems, affecting magma evolution and degassing and therefore ascent dynamics (e.g., Wallace and Edmonds, 2011). H_2O and CO_2 are the most abundant volatile components in magmas, followed by S components (principally SO_2 and H_2S) and halogens (mainly Cl, F).

S components generally receive particular attention due to their significant impact on atmospheric chemistry (e.g., Wallace and Edmonds, 2011) and Earth's average temperature (e.g., Robock, 2000). Indeed, sulphur released in the stratosphere during explosive volcanic

eruptions, mainly as SO_2 (Oppenheimer, 2003), forms sulphate aerosols, which may backscatter the incoming solar radiation, causing atmospheric cooling that may persist for months/years, as observed, for example, during and after the eruptions of Mt. Pinatubo (1991, e.g., Guo et al., 2004), Laki (1783-84, e.g., Thordarson and Self, 2003), Tambora (1816, e.g., Cole-Dai et al., 2009), Samalas (1257, e.g., Vidal et al., 2016), and Krakatoa (1883, e.g., Robock, 2000; and references therein).

In magmatic systems, the behaviour of sulphur is complex as it is linked to a multiplicity of parameters such as melt and volatile phase compositions, pressure, temperature, and redox conditions. Several experimental investigations have focused on the solubility of sulphur in hydrous silicic melts (e.g., Binder et al., 2018; Botcharnikov et al., 2004; Carroll and Rutherford, 1985, 1987; Carroll and Webster, 1994; Clemente et al., 2004; Luhr, 1990; Webster and Botcharnikov, 2011) and in hydrous basaltic melts (e.g., Beermann et al., 2011, 2015; Lesne et al., 2015; Luhr, 1990; Liu et al., 2007; Moune et al., 2009). These studies showed that sulphur solubility in silicate melts is influenced by melt composition and oxygen fugacity (fO_2). Melt polymerization is for instance an important parameter controlling the solubility of sulphur-bearing minerals (Masotta and Keppler, 2015) and the fluid-melt partitioning of sulphur (Masotta et al., 2016). Moreover, for a fixed composition, a decrease of temperature and pressure leads to a decrease in S solubility (e.g., Beermann et al., 2011; 2015; Lesne et al., 2011b; Webster and Botcharnikov, 2011).

The principal difficulty to constrain S behaviour in hydrous basaltic melts and, particularly, sulphur partitioning between the fluid phase and the silicate melt, is to evaluate its speciation as a function of the redox conditions. Experimental determinations clearly show that (i) sulphur dissolves in the melt primarily as sulphide species (S^{2-}) under reduced redox conditions, and mainly as sulphate species (S^{6+}) in more oxidized redox conditions (e.g., Fincham et al., 1954; Carroll and Rutherford, 1985, 1988), and (ii) sulphate species are

significantly more soluble than sulphide ones (e.g., Botcharnikov et al., 2011; Beermann et al., 2011, 2015; Carroll and Rutherford, 1985, 1987; Jugo et al., 2005; Luhr, 1990). The transition from sulphide- to sulphate- dominated systems occurs over a narrow fO_2 interval, roughly from NNO-0.5 to NNO+1.5 (Jugo et al., 2005; Jugo, 2009; Wallace and Carmichael, 1994), where NNO represents the Nickel-Nickel Oxide buffer that is calculated trough the equilibrium expression of Frost (1991) and is about 0.6 log units above the fO_2 of the FMQ (Fayalite-Magnetite-Quartz) buffer at the considered pressures and temperatures. Such redox conditions correspond to the fO_2 conditions prevailing in magmas from arcs (Parkinson and Arculus, 1999) back-arcs, island-arcs and oceanic islands (Ballhaus, 1993; Moussallam et al., 2019).

Melt inclusions (MIs) represent a crucial tool to provide information on the compositions and S content of primitive magmas (e.g., Collins et al., 2009; Corsaro and Métrich, 2016; Gennaro et al., 2019; Kamenetsky and Clocchiatti, 1996; Kamenetsky et al., 2007; Métrich and Clocchiatti, 1989; Métrich et al., 2004; Moretti et al., 2018; Salem et al., 2019; Schiavi et al., 2015; Spilliaert et al., 2006a). Olivine-hosted MIs can be used to investigate the fO_2 of their source region and to evaluate the redox variations of magmas during ascent and differentiation (e.g., Cottrell and Kelley, 2011; Hartley et al., 2017; Kelley and Cottrell, 2012; Moussallam et al., 2014, 2016).

Mt. Etna (Italy) was chosen as a case study, due to the association of S-rich basaltic magmas (up to > 4000 ppm S, Gennaro et al., 2019; Moretti et al., 2018) and high SO_2 fluxes (50,000 t in 2014, D'Aleo et al., 2016). The available estimations of the redox conditions of this magmatic system vary from NNO to NNO+1.8: phase equilibrium experiments on hawaiitic compositions (Mt. Maletto, 1983 and 1991-1993 eruptions; e.g., Armienti et al., 1994; Métrich and Rutherford, 1998; Trigila et al., 1990) suggest fO_2 of ~NNO; Cr-spinel and Fe-Ti oxides compositions in primitive basaltic compositions (Mt. Spagnolo and 2001 eruptions;

Kahl et al., 2011; Kamenetsky and Clocchiatti, 1996) indicate fO_2 varying between NNO and NNO+1.8; S speciation in melt inclusions (from 1989-1990, 2001, FS and Mt. Spagnolo eruptions; Métrich and Clocchiatti, 1996; Métrich et al., 2009; Morizet et al., 2017) suggests fO_2 between NNO+0.3 and NNO+1.

In order to improve the knowledge of S behaviour and redox conditions of Etnean magmas during differentiation and degassing, we couple the study of natural olivine-hosted MIs with an experimental investigation of S solubility in Etnean hydrous alkali basalts.

We highlight how magma differentiation affects redox conditions and sulphur degassing of Etnean magmas, explaining the variations from the most primitive MIs entrapped at depths > 10 km below sea level ("bsl") inside the plumbing system to the shallower and evolved MIs.

GEOLOGICAL BACKGROUND OF MT. ETNA

Mt. Etna is a basaltic, persistently active stratovolcano, situated on the boundary of the colliding African and European plates, close to the Aeolian subduction area (e.g., Branca et al., 2011; Clocchiatti et al., 1998). The activity started ~500 ka BP as a submarine volcano evolving toward an effusive/explosive aerial volcano. Sub aerial activity of Mt. Etna presents extremely variable styles, from effusive to highly explosive and caldera-forming (e.g., Branca et al., 2011). The last stage of Etnean volcanism (recent Mongibello, 3-5 ka, Branca et al., 2011) was marked by the alternation of lateral, eccentric or DDF ("Deep Dike Feed", Corsaro et al., 2009) activity producing primitive magmas, and central and/or sub-terminal eruptions with the emission of more evolved magmas. Among the DDF eruptions, the most studied is the highly explosive (sub-plinian) Fall Stratified (FS) eruption, which occurred 4 ka BP (Coltelli et al., 2005) and was characterized by an uncommon picritic magma.

By contrary, the majority of Etnean rocks have more evolved trachybasaltic compositions, and were erupted during either strombolian and paroxysmal activity at the summit craters (lava fountains and associated lava flows), or effusive to explosive flank eruptions, concurrently to the release of huge amounts of volatiles in the atmosphere (Aiuppa et al., 2008). Indeed, Mt. Etna is an important emitter of volatiles in the atmosphere, with an estimated average total flux of ~ 21000 t day^{-1} during the 2005-2006 eruptive period (Aiuppa et al., 2008). Among the major volatile species (H_2O, CO_2, S species), SO_2 is probably the most accurately measured in the Etnean plume (Aiuppa et al., 2005, 2008; D'Aleo et al., 2016; Delle Donne et al., 2019; McGonigle et al., 2003; Salerno et al., 2009). D'Aleo et al. (2016) estimated up to ~50000 t of SO_2 during the 2014 eruption, and important SO_2 fluxes are observed also during non-eruptive periods (~3563 t day^{-1}; Salerno et al., 2009). Yet, these high SO_2 emissions are not fully constrained in terms of S origin and S behaviour during magma ascent and evolution.

Extremely debated is also the geochemical variability (e.g., increase of alkali, mainly K_2O, and radiogenic elements) in the recent Etnean magmas, as observed from isotopic and elemental geochemical data on rocks and melt inclusions (e.g., Correale et al., 2014; Corsaro and Métrich, 2016; Di Renzo et al., 2019; Gennaro et al., 2019; Schiavi et al., 2015; and references therein). For example, the post-1971 enrichment in alkalis (K, Rb, Cs) and radiogenic Sr and B elements (e.g., Allard et al., 2006; Armienti et al., 2004; Ferlito and Lanzafame, 2010; Métrich et al., 2004) has been ascribed alternatively to (i) the interaction between an OIB-type (or HIMU-type) mantle source and an enriched component (EM1), corresponding to a slab-modified mantle or to (ii) the mixing between mantle-derived magmas and a K- and Si-enriched melt (Schiano and Clocchiatti, 1994). On the other hand, Gennaro et al. (2019) proposed that part of the variability of major elements and volatiles observed in the Etnean magmas of the last 15 ka could be ascribed to differentiation processes

of a primitive FS-type magma, occasionally accompanied by secondary source-related and/or crustal processes.

SAMPLES AND METHODS

Etnean melt inclusions

Eleven olivine hosted MIs from tephra of the FS sub-plinian DDF eruption were characterized for their chemical compositions and volatile contents, as well as Fe speciation.

FS tephra spreads mostly in the east and north flanks of the Etnean volcano, reaching a maximum thickness of 110 cm 7 km away from the summit craters. This rock (phenocrysts ≤10 vol%) has a picro-basaltic composition (MgO =17 wt%, Gennaro et al., 2019), and contains euhedral $Fo_{89–91}$ olivine (up to ~ 5 mm in size), subhedral clinopyroxene and rare Cr-spinel, as microphenocrysts and/or included in olivine (e.g., Correale et al., 2014; Corsaro and Métrich, 2016; Gennaro et al., 2019; Kamenetsky et al., 2007).

The MIs from FS products have already been characterized for their chemical compositions and volatile contents (Corsaro and Métrich, 2016; Gennaro et al., 2019; Kamenetsky et al., 2007). They are highly primitive (up to 12 wt% MgO) and show particularly high volatile contents, with H_2O up to 6 wt.%, CO_2 up to > 5000 ppm, S up to 3550 ppm, and Cl up to > 3000 ppm. Entrapment depths calculated from H_2O and CO_2 contents range between 2 and 16 km bsl (Gennaro et al., 2019) indicating that FS MIs are probably the most representative samples of the redox state of deep and primitive magmas.

In order to constrain the redox state of shallower and more evolved magmas, some olivine-hosted MIs from Mt. Spagnolo (~4-15 ka BP), 2002-2003, 2006, 2008 and 2013 eruptions, previously analysed by Gennaro et al. (2019), have been also investigated by XANES spectroscopy. Unfortunately, only few MIs were analysable: 1 MI from Mt. Spagnolo lava, 2

MIs from 2002/3 tephra, 1 MI from 2006 tephra, 2 MIs from 2008/9 tephra, and 3 MIs from 2013 lavas, the latter emitted during a paroxysmal event that contributed to produce the new South-East crater.

Mt. Spagnolo lavas, produced by a DDF eruption, are located about 6 km north-west of the central crater. Mt. Spagnolo products present primitive characteristics, i.e. high CaO/Al_2O_3 up to 1, olivine with $Fo_{74–89,}$ presence of Cr-spinel, high Sr content and $^{87}Sr/^{86}Sr$ ratios (e.g., Armienti et al., 1988; Correale et al., 2014; Gennaro et al., 2019; Kamenetsky and Clocchiatti, 1996).

The 2002/2003 eruption was a DDF eruption, occurring along both the south and the north rift (eastward to the central craters), producing rocks with basaltic (around south rift) to evolved trachybasalt composition (e.g., Spilliaert et al., 2006a, 2006b). The MIs investigated for Fe speciation are from tephra sampled along the south rift (and thus named "2002S", Gennaro et al., 2019). The other investigated MIs are from tephra produced during the eruptions of 2006 (sub-terminal activity near the South-East crater), from bombs produced during intense explosions that occurred in the North-East crater in 2008/2009, and from lava emitted during a paroxysm that occurred at the New South-East crater in 2013 (Gennaro et al., 2019). These trachybasalts have a more evolved compositions, with respect of 2002S and all Mt. Spagnolo and FS rocks (e.g., Gennaro et al., 2019).

Experimental methods

The starting material was prepared from the Mt. Spagnolo lava, which is one of the most primitive basalts known to have erupted at Mt. Etna (e.g., Correale et al., 2014; Gennaro et al., 2019; Kamenetsky and Clocchiatti, 1996). The rock was finely ground, melted in a Pt crucible at 1400 °C and 1 atm for 3 hours, and rapidly quenched, in order to produce a degassed crystal- and bubble-free starting glass (composition given in Table 1).

The experiments were carried out in a vertically-operating internally-heated pressure vessel (IHPV) at the *Institut des Sciences de la Terre d'Orléans (ISTO,* France). Platinum capsules (2.5 mm inner diameter, 0.2 mm wall thickness, 20 mm length) were used as containers. Compared to other metals and alloys such as AuPd or Pd (Le Gall, 2015; Lesne, 2008; Pichavant et al., 2006), Pt is preferred for experiments performed at temperatures higher than 1050 °C and is less reactive with sulphur. It forms Fe-Pt sulphides at the capsule rim that generally lower the Fe content of the melts during experiment. We compensated for iron loss to the Pt capsule by adding variable amounts of FeO (0 to 6 wt%; Table 2) to the starting glass (Brugier et al., 2015; Le Gall, 2015), while limiting the run duration as much as possible.

About 50 mg of powdered starting glass were loaded into Pt capsules, together with variable amounts of FeO, H_2O, S, and CO_2 (Table 2). Sulphur was added as elemental S (1-4 wt%, Table 2), and water as distilled H_2O. Both CO_2-free and CO_2-bearing charges (where CO_2 was added as dehydrated oxalic acid, $C_2H_2O_4$*$2H_2O$) were prepared, keeping the mass fraction of fluid component (H_2O+CO_2) to ~10 % of the total mass of the charge (i.e. including volatiles, glass and sulphur, Table 2).

For each experimental run, up to 4 capsules were placed in the hotspot of the molybdenum furnace, and their temperature (T) was monitored with two S-type thermocouples (uncertainty ± 5 °C) placed at the top and the bottom of the capsules. The T gradient along the capsules was always less than 10 °C. Ar was used as pressurizing medium and was mixed with variable amounts of H_2 in order to vary the fO_2. Total pressure was recorded by a transducer calibrated against a Heise Bourdon tube gauge with an uncertainty ± 20 bars. The experiments were performed at 1200 °C and between 180 and 210 MPa, and lasted between 2 and 3 hours, in order to ensure the attainment of equilibrium between the basaltic melt and the fluid phase (e.g., Jugo et al., 2005). This duration is sufficient to ensure homogeneous sulphur content in

the silicate melts at the investigated temperature. Longer durations were found to corrode the Pt capsule and pierce it (Le Gall, 2015). All experiments were ended by a drop quench (estimated cooling rate of about 100 °C/s; Di Carlo et al., 2006).

The aim of this experimental investigation was to confirm the effect of fO_2 on S behaviour at conditions relevant to those of the Etnean magmatic system in terms of volatile and FeO contents.

Redox conditions in each capsule were monitored using the solid sensor method, consisting of two pellets of metallic Co and Pd mixed with CoO (each pellet having a different starting Co_0/Pd_0 ratio), placed in a separate Pt capsule containing 15 wt% H_2O (Pownceby and O'Neill, 1994; Taylor et al., 1992). Since CoPd may alloy with Pt, the redox sensitive pellets were isolated from the capsule walls, by a sleeve of ZrO_2 powder. As Pt capsules are highly permeable to H_2 at elevated temperatures, the hydrogen fugacities of sensor and sample capsules are the same ($fH_{2(sensor)} = fH_{2(sample)}$; Taylor et al., 1992). After experiment, analysis of CoPd (Xco = 0.19±0.05, Table 2) alloys coexisting with CoO allows the fO_2 of the sensor to be determined (Pownceby and O'Neill, 1994). Then, $fH_{2(sensor)}$ and $fH_{2(sample)}$ are calculated from the water dissociation equilibrium equation $\log fH_2 = \log fH_2O - 1/2 \log fO_2 - \log K_w$, where K_w is the dissociation constant of water (calculated from Robie et al., 1979) and fH_2O is the fugacity of pure H_2O at experimental P and T (calculated from Holloway, 1987), see also Pichavant et al. (2014).

For a given experimental run (constant P-T-fH_2), the fO_2 within each capsule varies along with its H_2O fugacity (fH_2O), which was determined for each charge from the H_2O content of the quenched glass, using the thermodynamic model for H_2O solution in multicomponent melts of Burnham (1979). Then, the fO_2 in each charge is calculated from the water dissociation equilibrium equation above. Results of the fO_2 calculations are given in Table 2. Typical uncertainties on $\log fO_2$ range between 0.12 and 0.47 log units, propagated from an

uncertainty of ± 0.5 bar absolute on P_{H_2} (P_{H_2} is the pressure of H_2 gas initially loaded in the vessel at room temperature). The uncertainty on fO_2 therefore increases with decreasing P_{H_2}, being higher for the oxidized (lowest P_{H_2}) than for the reduced redox conditions (highest P_{H_2}) experiments.

Calculation of volatile contents in the fluid phase and S fluid/melt partitioning coefficients

The amount of sulphur (and other volatiles) contained in the fluid phase of the experimental capsules was estimated following the procedure described in Beermann et al. (2015). Firstly, (i) the mass of i^{th} volatile species in the melt phase (mi_{melt}) was determined in order to calculate (ii) the respective masse in the fluid phase (mi_{fluid}):

$$\text{(i) } m\ i_{melt} = ci_{melt} \cdot m_{glass} \,/\, 100 - \Sigma c\ vol_{melt}$$

$$\text{(ii) } m\ i_{fluid} = m\ i_{bulk} - m\ i_{melt}$$

where m_{glass} is the initial starting material mass, ci_{melt} [wt%] is the concentration of each volatile ($S+H_2O\pm CO_2$) dissolved in the melt phase (details on the estimation of volatiles in melt are given in the following section), $\Sigma c\ vol_{melt}$ [wt%] is the total sum of volatile components dissolved in melt; mi_{bulk} is the initial added quantity of each (i) volatile species. Finally, the S concentration (cS_{fluid} [wt%]) in the fluid phase was determined as follows:

$$cS_{fluid} = (mS_{fluid} \times 100) \,/\, \Sigma\ m\ vol_{fluid}$$

where $\Sigma m\ vol_{fluid}$ is the sum of the calculated mass of volatiles in the fluid phase and mS_{fluid} is the mass of S in the fluid phase as calculated before. Therefore, $DS^{fluid/melt}$ ($= S_{fluid}/S_{melt}$; concentration in wt%) is calculated using the amount of sulphur dissolved in the experimental glasses (S_{melt}) and the calculated sulphur exsolved in the fluid phase (S_{fluid}). Errors associated with the amount of S_{fluid} and the value of $DS^{fluid/melt}$ have also been estimated by using the calculation proposed by Beermann et al. (2015).

Analytical methods

Melt inclusions in olivine crystals and experimental products, mounted in epoxy resin, were imaged with two scanning electron microscopes (SEM): a Tescan MIRA 3 XMU (BRGM, Orléans), using 25 kV electron energy, and a Zeiss Merlin Compact (ISTO, Orléans), using 15 kV electron energy. Semi-qualitatively analyses of sulphide droplets were also performed with these SEM devices.

Major elements, S and Cl concentrations in melt inclusions, olivine phenocrysts and experimental glasses were determined with a Cameca SX FIVE electron microprobe (EMP, at ISTO, Orléans) operated under an acceleration voltage of 15 kV, a beam current of 6 nA and a peak counting time of 10 s for all elements, except S (60 s). The metallic alloys of the sensors were analysed with an acceleration voltage of 20 kV and a beam current of 20 nA. The Pt capsule walls were also analysed for their Fe and S contents, using an acceleration voltage of 20 kV and 30 nA beam current. A focused beam was used for olivine and metals, while beams of 2-6 and 6-12 μm were used respectively for melt inclusions and experimental glasses, to reduce Na migration. Natural minerals and oxides were used as standards (Na and Si: albite, K: anorthoclase, Ca: anhydrite, P: apatite, Cl: vanadinite, Mg: MgO, Al: Al_2O_3, Fe: Fe_2O_3, Ti and Mn: $MnTiO_3$, Pt: metal Pt); S was calibrated against barite ($BaSO_4$).

H_2O and CO_2 contents in the glass phase of the FS doubly-polished MIs were determined by Fourier transform infrared spectroscopy (FTIR) using a Nicolet 6700 Magna spectrometer equipped with an IR microscope and an MCT detector (ISTO, Orléans). The thickness of each chip (27–56 μm) was assessed using a petrographic microscope, through repeated measurements. For each melt inclusion, at least two spectra were acquired to check the homogeneity of dissolved volatile contents. Absorption spectra were acquired in the range 1000–6000 cm^{-1} with 128/560 scans and a resolution of 4 cm^{-1}, using a Globar internal IR

source and a KBr beam-splitter. The H_2O and CO_2 concentrations (C) were calculated respectively from the absorbance (A) of the 3530 cm^{-1} (total H_2O) and of the 1430 and 1525 cm^{-1} doublet (CO_3^{2-} bending) bands, using the modified Beer-Lambert law (Stolper, 1982):

$C = ((MW \cdot A)/(d \cdot l \cdot \varepsilon) \cdot 100)$

where MW is the molecular weight (g/mol), d the melt density (g/l), ε the molar absorption coefficient ($l \cdot mol^{-1} \cdot cm^{-1}$), l the optic path (i.e. the thickness of the glass sample, cm). A molar extinction coefficient (ε) of 63 $l \cdot mol^{-1} \cdot cm^{-1}$ was used for the 3530 cm^{-1} band (Dixon et al., 1988), whereas the coefficient for the 1525 cm^{-1} band (415±4 $l \cdot mol^{-1} \cdot cm^{-1}$) was calculated for each MI on the basis of the Na/(Na+Ca) molar ratio of the melt, using the Dixon and Pan (1995) method.

The absorbance values of the carbonate doublet were estimated after subtraction of a spectrum of a CO_2-free synthetic glass with similar composition and H_2O content (Lesne et al., 2011a). The density of natural glasses (2.70±0.03 $g \cdot cm^{-3}$) was calculated from the density of the starting anhydrous basaltic experimental glass (2.78 $g \cdot cm^{-3}$, Gennaro, 2017). The effect of dissolved water was accounted for using the method of Richet et al. (2000) and CO_2 was assumed to have no influence on the glass density (Bourgue and Richet, 2001).

For experimental glasses, H_2O and CO_2 contents were determined by secondary ion mass spectrometry (SIMS), using both a Cameca IMS 1270 and a Cameca IMS 1280 HR2 instruments (*Centre de Recherches Pétrographiques et Géochimiques*, Nancy, France). Experimental and standard glasses were pressed into indium within an aluminium disk, and then gold coated and outgassed in the SIMS chamber until a pressure of 10^{-8}-10^{-9} Torr was reached. The acquisition, preceded by 30 s pre-sputtering period (to remove impurities from the sample surface), was performed using a Cs^+ primary beam of 5 nA, with an impact energy of 20 kV in 12–15 cycles. Glasses with compositions similar to the Etna samples including N72 basalt from Kamchatka and KL2-G basalt from Kilauea (H_2O = 0-4.2 wt% and CO_2 = 0-

3172 ppm; Jochum et al., 2006; Shishkina et al., 2010) were used as standards. The signals for $^{12}C^-$ and $^{16}O^1H^-$ were gathered in monocollection mode during the same analysis (acquisition time of 12 min). Concentrations of CO_2 were calculated by comparing the $^{12}C^-/^{28}Si^-$ vs. SiO_2 of the sample with that of the reference glass. H_2O was calculated by comparing the OH^-/H^- vs. H_2O in the reference materials with the obtained OH^-/H^- of the sample.

The H_2O and CO_2 of MIs from Gennaro et al. (2019) had been estimated by SIMS, following the same procedure described above.

XANES $Fe^{3+}/\Sigma Fe$ investigation

The pre-edge structure of the Fe K-edge (Fig. A1 in Supplementary Data Electronic Appendix_1) was investigated in 21 double-polished MIs, one matrix glass and one embayment from this study (FS) and from Gennaro et al. (2019; FS, Mt. Spagnolo, 2002-2013 eruptions) and 6 experimental glasses by X-ray Absorption Near Edge Structure (XANES) at the Diamond Light Source (DLS, Oxfordshire), using the I18 beamline over the energy range 7020-7500 eV, in order to determine the $Fe^{3+}/\Sigma Fe$ ratio. During the analytical acquisition, the storage ring was operating at 3 GeV with an electron current of about 300 mA.

XANES spectra were acquired during two analytical sessions. In a first session (in 2015), 7 MIs (from Mt. Spagnolo, 2002/2003, 2006, 2008/2009, 2013 eruptions), 1 embayment (from 2006) and 1 matrix glass (2002/2003 eruption) from Gennaro et al. (2019) were analysed using methods described in Moussallam et al. (2014, 2016).

The X-rays were focused with Kirkpatrick–Baez mirrors down to 2 μm (horizontal) × 2.5 μm (vertical) beam size. The beamline utilizes a liquid nitrogen-cooled double-crystal monochromator with silicon crystals, and Si (333) reflection was used to increase the energy resolution. Measurements were performed in fluorescence mode, the energy-dispersive detector used was a 6-element SGX Sensortech silicon drift detector positioned at 90 degrees

with respect to the incident X-ray beam. The sample was positioned such that the normal to its surface was tilted 10 degrees relative to the incident X-ray beam in order to improve the horizontal resolution and reduce potential self-absorption effects. The incident X-ray beam was filtered with Al foils (varying in thickness from 0.025 to 0.1 mm) with the aim to keep the detector count rate within the linear response region and to remove the effect of beam damage on the sample. The energy step sizes and dwell times used are given in Table A1 (Supplementary Data Electronic Appendix _1).

In a second session (in 2018), XANES spectra were collected for the 6 experimental glasses and the 11 MIs from FS tephra characterized in this study, along with 3 MIs from Gennaro et al., 2019 (1 MI from 2002/2003, 1 from 2013 and 1 MI from FS eruptions) following the methodology described in Moussallam et al., (2019). The X-rays were focused with Kirkpatrick-Baez mirrors down to 2 μm (horizontal) × 1.2 μm (vertical) beam size. Measurements were performed in fluorescence mode using two energy-dispersive Vortex ME-4 silicon drift detectors positioned 45 degrees to the incident beam (one located directly above the other and pointing towards the sample). The sample was positioned so that the normal to the sample surface was at 45 degrees to the incident X-ray beam. The incident X-ray beam was filtered with an Al foils of 0.25 mm thickness to remove the effect of beam damage on the sample (see Supplementary Data Electronic Appendix_1). The energy step sizes and dwell times used during the 2018 session are the same as those used for the 2015 acquisition (Table A1 in Supplementary Data Electronic Appendix _1). For the MIs, two spectra were acquired and co-added for each analysis.

In total, during both sessions, 52 MIs were exposed to XANES beam, but many spectra exhibited olivine contamination (Fig. A2, Supplementary Data Electronic Appendix _1) and other analytical problems, and thus were not further considered.

The NMNH 117393 dry basalt glasses, loaned by the Smithsonian Institution National Museum of Natural History, were used as reference and their spectra were acquired under the same conditions as applied to the investigated samples during both sessions. Their $Fe^{3+}/\Sigma Fe$ ratios have been measured by Mössbauer spectroscopy (Cottrell et al., 2009, Zhang et al., 2018). The reference glasses were analysed at the beginning and end of each session and an average spectrum for each glass was used to derive the calibration curve (see Supplementary Data Electronic Appendix_1 for details on calibration and data processing).

RESULTS

Experimental charges

Experimental products are brown, uniformly coloured and crystal-free glasses (Fig. 1a), except for the presence of small sulphide globules (< 3 μm in diameter, Fig. 1b) in the most reduced runs (fO_2< NNO+1). Their size did not allow EMP analysis, but semi-qualitative SEM-EDS spectra indicate that they are mainly constituted of Fe, Pt and S. Rare microbubbles are observed in the melt, whereas larger bubbles are frequently located at the glass-capsule interface (Fig. 1a), indicating fluid saturation. The presence of a free fluid phase in each experimental capsule was corroborated by the weight loss after piercing the capsules at the end of the experiment.

The internal walls of all Pt-capsules present a rim of Pt-Fe-S aggregates, which thickness range from ~10 up to 80 μm. SEM imaging (Figs. 1c-d) shows that, for a given run, the thickest reaction rims are for the charges with CO_2 and in which the highest amounts of S were added.

Major element compositions and volatile contents

Major element compositions and volatile contents of the 14 basaltic experimental glasses are reported in Table 3. Measured standard deviations for major elements are generally low (Table 3), indicating homogeneous compositions.

Dissolved H_2O content range from 3.3 and 5.2 wt% (Table 3) with the lowest concentrations (< 4 wt%) in the CO_2-bearing glasses (SPA 1702#5, 2703#3, 2703#4, 2704#4) which contain between 767 to 1618 ppm CO_2. The dispersion in the H_2O and CO_2 measurements is very low (0.02-0.22 wt% and 8-27 ppm, respectively), signifying that the experimental glasses contain homogeneous concentrations of dissolved H_2O and CO_2.

The sulphur content of the experimental glasses varies from 711 to 6039 ppm, with standard deviations between 84 and 300 ppm (Table 3). The only two parameters that were varied in our experimental runs (Table 2) and that affect the S content of the silicate melt are FeO_{tot} and fO_2 (e.g., Jugo et al., 2005; Lesne et al., 2015; Zajacz et al., 2012). Considering experimental glasses with similar FeO_{tot} content, oxygen fugacity is confirmed to be the main parameter affecting sulphur solubility in our experiments (Fig. 2a), in agreement with previous studies (e.g., Jugo et al., 2005, and reference therein). We cannot evaluate the role of melt composition on the S content of our glasses, given the extremely low variability of major element compositions. Only the FeO_{tot} content varies from 5.9 to 10.1 wt % (Table 3), but no clear correlation with the S content is observed (Fig. 2b), most likely owing to the effect of fO_2. When considering samples within a narrow range of fO_2 (between NNO+0.5 and NNO+0.6), a slight positive correlation between S and FeO_{tot} contents can be noted (Fig. 2b). No clear relationship is observed between the S and the H_2O contents of our experimental glasses (Fig. 2c); neither between S and CO_2 contents (Fig. 2d), probably due to the more important effect of fO_2. Previous studies have proposed either a positive (e.g., Fortin et al., 2015; Moune et al., 2009) or a negative effect (Li and Ripley, 2009; Liu et al., 2007) of the water content on the sulphur content at sulphide saturation (SCSS). Moretti and Baker (2008)

suggest that the effect of water on SCSS can be variable, depending on pressure and melt compositions. We do not participate in this debate, given that our experiments show that the effect of fO_2 largely overwhelm the effects of FeO and H_2O contents on SCSS. To model the behaviour of S during ascent and crystallization of Etnean magmas, we will therefore point out the effect of fO_2 and neglect those of melt composition, including H_2O content.

Fluid/melt partitioning of sulphur

The amount of sulphur dissolved in the melt (S_{melt}, in wt%, Table 3) and that calculated in the fluid phase of the experiments (S_{fluid}, in wt%, Table 3 and in Fig. S1 in Supplementary Data Electronic Appendix_2) are used for calculating the S fluid/melt partitioning coefficient ($DS^{fluid/melt} = S_{fluid}/S_{melt}$; Table 3). The presence of sulphide globules and the Pt-Fe-S alloy at the internal capsules walls is neglected in the calculation of the S_{fluid}, like in previous studies (e.g., Beermann et al., 2015; Le Gall, 2015; Lesne et al., 2015), due to the difficulty of evaluating their abundances. Calculated $DS^{fluid/melt}$ values are therefore maximal values, because S contained in these phases is implicitly included into S_{fluid}. Due to this problem, the values of $DS^{fluid/melt}$ calculated for samples showing thick Pt-Fe-S aggregates at the capsule rim were not selected for our modelling. We used the approach described in Alletti et al. (2009) to refine this selection and check whether the calculated $DS^{fluid/melt}$ values unequivocally indicate the partition of S between the fluid and melt phases or if they are strongly perturbed by S loss either in the sulphide phase (Fe-Pt-S globules in melt) and/or at the capsule wall. In a plot S_{melt} versus S_{fluid} (Fig. S1a in Supplementary Data Electronic Appendix_2) it is observed that for glasses with dissolved $S_{melt} < 2500$ ppm, the calculated S_{fluid} increases strongly (10 to 40 wt%), whereas S_{melt} is almost constant (0.1-0.2 wt%), indicating that in these runs an additional S-bearing phase sequesters a significant part of S of the system (Alletti et al., 2009 and references therein).

The selected $DS^{fluid/melt}$ values range between 50±4 and 146±6 (Fig. 3, Table 3) and are in the range of previous experimental estimates on Etna trachybasalts (1-236, Beermann et al., 2015) and on other basalt compositions (7-2814, Fiege et al., 2015; Le Gall, 2015; Lesne et al., 2011b; Zajacz et al., 2013).

Since our experimental P-T conditions and melt composition are constant, the only parameter affecting $DS^{fluid/melt}$ is fO_2. Among the selected values, $DS^{fluid/melt}$ decreases with increasing fO_2 (Fig. 3, red cross-shaped symbols), the lowest $DS^{fluid/melt}$ value (50±4) corresponding to the samples with the most oxidized redox conditions (fO_2 = NNO+1.7±0.5). Previous works also suggest the influence of pressure and temperature on the $DS^{fluid/melt}$ (e.g., Lesne et al., 2011b; Webster and Botcharnikov, 2011). Pressure and $DS^{fluid/melt}$ are generally inversely correlated (Lesne et al., 2011b). The relation with temperature remains unclear; only the decompression and annealing experiments of Fiege et al. (2015) show an inverse relation between $DS^{fluid/melt}$ and T, in the 1150-1250 °C range.

Considering our results and a selection of data previously published (Beermann et al., 2015; Le Gall, 2015; Lesne et al., 2011b; Zajacz et al., 2013), we calibrated, for a basaltic magma, an empirical model for the dependence of $DS^{fluid/melt}$ with fO_2, P, and T:

$$\text{Log}\,(DS^{fluid/melt}) = a/\text{T} + b\text{P} + c\Delta\text{NNO} + d \qquad [1]$$

where T is in °C, P in MPa, a= -7621.011, b= -0.0016, c= -0.462, d= 9.117 (Table S1 in Supplementary Data Electronic Appendix_2).

The selected dataset used for this model includes basaltic glasses quenched at T=1030-1200 °C, P= 25-300 MPa, and log fO_2 between NNO-0.8 and NNO+2.4, chosen with the same criterion used for our data (as in Alletti et al. 2009). We used the data from Beermann et al. (2015), which have an Etnean composition, excluding (i) the glasses in which the presence of a S-bearing phase is important (those with anomalous correlation between S_{fluid} and S_{melt}

concentration, as described above) and (ii) those with unrealistically (for Etna) high Cl content.

We also considered the data of the decompression experiments from Le Gall (2015) and Lesne et al. (2011b), performed with Stromboli and Masaya basaltic compositions (selected with the approach as above). The data from the decompression (*plus* annealing) experiments of Fiege et al. (2015), also shown in Figure 3, are excluded from our empirical $DS^{fluid/melt}$ model, because, even those approaching to near-equilibrium conditions show a negative correlation in the S_{fluid} vs S_{melt} concentration plot (not shown).

Figure 3 shows the selected values of $DS^{fluid/melt}$ used for the proposed empirical model. Our data highlight the relation between $DS^{fluid/melt}$ and fO_2 at constant T (1200 °C) and P (~ 200 MPa). The other data corroborate this relation despite the variability of P and T conditions. Figure 3 also shows the curves of $DS^{fluid/melt}$ versus fO_2 calculated by the model *[1]* at various T-P conditions. The model predicts that fO_2 and T more significantly affect $DS^{fluid/melt}$ values than P (Fig. 3). Notably, the effect of a decrease in both fO_2 and P is to increase $DS^{fluid/melt}$; this increase can be partially counterbalanced by a decrease of T.

Modelled $DS^{fluid/melt}$ as function of T, P and fO_2 gives a coefficient of determination (R^2) of 0.79 (Fig. S2 in Supplementary Data Electronic Appendix_2). The large uncertainty in the estimation of both the experimental fO_2 and the amount of S in the experimental fluid phase (mainly due to the occurrence of sulphide phases), along with differences in the basaltic compositions and in the experimental set up prevents further improvement of this best fit.

$Fe^{3+}/\Sigma Fe$ ratio of the experimental glasses

The $Fe^{3+}/\Sigma Fe$ ratios of experimental glasses, measured by XANES, range from 0.22 to 0.27 (Table 2), with a precision (1σ) of 0.013. These values are generally lower than those calculated from the fO_2 imposed in the experiment (named "*experimental*" in Table 2 and Fig.

4), using the empirical formulation of Kress and Carmichael (1991), which relates $Fe^{3+}/\Sigma Fe$ ratios to fO_2, accounting for the chemical composition of the silicate melt, pressure and temperature:

$$(XFe_2O_3/XFeO) = a \ln(fO_2) + b/T + c + \Sigma d_i X_i + e\,[1\text{-}T_0/T - \ln(T/T_0)] + fP/T + g((T\text{-}T_0)P)/T + h\,P^2/T \quad [2]$$

where *a, b, c, d, e, f*, *g* and *h* are constants, *X*i are mole fractions of oxide components in silicate melts, T and P are in Kelvin and kbar, respectively, and T_0 is fixed to 1673 °K. However, the observed discrepancy (Fig. 4) is comparable to the typical uncertainty on *experimental* $Fe^{3+}/\Sigma Fe$ ratios, which varies between 0.010 and 0.052, with increasing redox conditions glasses (see "*Experimental methods*" section).

Melt inclusions

Primitive melt inclusions from FS eruption

MIs, entrapped in $Fo_{90\text{-}91}$ olivine phenocrysts from the FS scoria, have spherical and oval shapes (48-225 μm size), with typical scalloped edges (Figs. 5a-b; Kamenetsky et al., 2007). They consist of transparent glass, and contain spherical bubbles (Fig. 5a), with calculated V_b/V_{MI} ratios (bubble volume / MI volume) between 0.03 and 0.12 (Table 4). It cannot be excluded that these bubbles contain a substantial fraction of volatiles (especially CO_2) initially dissolved in the entrapped melt (e.g., Frezzotti, 2001; Moore et al., 2015; Robidoux et al., 2017; Wallace et al., 2015). Therefore, analysis of the glass only gives minimum volatile concentrations in the parent melt. Some MIs exhibit very small opaque oxides (Cr-Mg spinels) as previously found in other inclusions from the same deposit (Gennaro et al., 2019).

The chemical compositions of the investigated FS MIs, together with their volatile abundances, are reported in Table 4. The major element compositions have been corrected for post-entrapment crystallization (PEC %, Table 4) following Gennaro et al. (2019), and

references therein. Volatile contents are not corrected for PEC, as this would increase measured volatile contents only by relatively low amounts that are comparable to analytical uncertainties (Gennaro et al., 2019).

As already shown by previous studies (Corsaro and Métrich, 2016; Gennaro et al., 2019; Kamenetsky et al., 2007), MIs of the FS eruption present high CaO (11.9-16.3 wt%) and MgO (8.6-10.9 wt%) contents, high CaO/Al_2O_3 ratio (0.9-1.5), low alkali contents (2.6-4.1 wt%), and high volatile abundances (H_2O = 1.9-5.9 wt%, CO_2 = 687-2786, S = 235-3445; Cl = 1165-3123 ppm). These chemical features identify FS MIs as the most primitive Etnean melts determined so far.

These FS MIs are used for the Fe speciation investigation (see following section), together with other Etnean MIs and one embayments, already characterized by Gennaro et al. (2019) for their major element compositions and volatile contents (Table 4). These samples belong to Mt. Spagnolo (Fo_{82}), 2002/2003 (Fo_{72-74}), 2006 (Fo_{70-81}), 2008/2009 (Fo_{69-75}) and 2013 (Fo_{70-72}) eruptions (Figs. 5c-d), and have volatile contents generally lower than FS MIs (Table 4). Nevertheless, MIs from 2006 and Mt. Spagnolo eruptions have been shown to bear the highest S content (~ 4000 ppm, Gennaro et al., 2019; Moretti et al., 2018), among all the investigated MIs. Unfortunately, the MIs with the highest volatile contents were not available or had strongly olivine-contaminated XANES signals.

$Fe^{3+}/\Sigma Fe$ ratios of the MIs

$Fe^{3+}/\Sigma Fe$ ratios measured by XANES in the double-polished MIs range from 0.168 to 0.358 (Table 5, Figs. 6-7): FS MIs exhibit the highest $Fe^{3+}/\Sigma Fe$ ratios (0.274-0.358), whereas 2008-2013 MIs generally have the lowest values (0.168-0.225).

$Fe^{3+}/\Sigma Fe$ ratios do not show any clear relation with the estimated percentage of PEC (Fig. S3 in Supplementary Data Electronic Appendix_2), therefore, an important effect of post-

entrapment crystallization on the estimated $Fe^{3+}/\Sigma Fe$ can be excluded. Nevertheless, following the approach of Hartley et al. (2017), which estimates the effect of olivine crystallisation in the MI wall on the Fe^{3+} of the entrapped melt, we have corrected the $Fe^{3+}/\Sigma Fe$ for PEC (Table 4). For the MI with the highest PEC (14 %), the $Fe^{3+}/\Sigma Fe$ ratio would be lowered by an absolute value of 0.06 with respect to the estimated XANES value. Other mechanisms, such as H^+ diffusion through olivine or volatile loss (e.g., Bucholz et al., 2013; Danyushevsky and Plechov, 2011; Frezzotti, 2001; Gaetani and Watson, 2000), could modify the $Fe^{3+}/\Sigma Fe$ ratio of the melt after its entrapment. The H^+ diffusion trough the olivine crystal could result in the oxidation of the system and the formation of magnetite dust (e.g., Danyushevsky et al., 2002; Frezzotti, 2001), which is not found in the investigated MIs.

Among the investigated melt inclusions, high values of PEC are estimated for both Mt. Spagnolo and FS (Table 4). We used an independent oxybarometer (Ballhaus et al., 1990, 1991) to estimate the fO_2 of Mt. Spagnolo and FS magmas from mineral equilibria (see next section), and show that post-entrapment modifications of the $Fe^{3+}/\Sigma Fe$ ratio are likely to be negligible.

The $Fe^{3+}/\Sigma Fe$ ratios generally decrease with decreasing CaO/Al_2O_3 ratios and MgO content (Figs. 6a-b), and with increasing K_2O, Na_2O and SiO_2 contents (Figs. 6c-d-e). Less clear is the variation with the FeO_{tot} (Fig. 6f), suggesting an influence of the crystallization of Fe-bearing minerals on the $Fe^{3+}/\Sigma Fe$ ratio. No clear correlation is visible between $Fe^{3+}/\Sigma Fe$ ratios and abundances of H_2O, S, Cl and CO_2 (Fig. 7), nor with the estimated storage pressure (Fig. 8). Only FS MIs generally show higher H_2O, CO_2 and S contents and $Fe^{3+}/\Sigma Fe$ ratios than more evolved MIs (Fig. 7). These observations suggest that the variation of the melt $Fe^{3+}/\Sigma Fe$ ratio is negligibly affected by decompression and degassing.

Redox conditions of Etnean magmas

$Fe^{3+}/\Sigma Fe$ ratios determined by XANES for the MIs of FS, Mt. Spagnolo and 2002-2013 eruptions (Table 5) are used for estimating the redox conditions of the magmas feeding these eruptions, through the equation *[2]*.

Oxygen fugacity estimations for Etnean MIs are reported in Table 5, expressed as deviation from the NNO buffer (ΔNNO). For these calculations, we used the pressure values estimated from the H_2O-CO_2 contents (Table 4), and temperatures of 1200 °C for FS (Mollo et al., 2015), 1170-1180 °C for Mt. Spagnolo (Kamenetsky and Clocchiatti, 1996) and 1130-1150 °C for the other eruptions (e.g., Kahl et al., 2011, 2015; Mollo et al., 2015).

FS MIs show the highest values (NNO+0.7 to NNO+1.6), together with the only MI from Mt. Spagnolo eruption (NNO+1.4), whereas the lowest values (NNO-0.9 to NNO-0.2) are observed for MIs from 2008 and 2013 eruptions (Fig. 9a).

Previous studies estimated redox conditions between NNO and NNO+1.8 (Fig. 9b), based on phase-silicate melt and phase-phase equilibria (e.g., Armienti et al., 1994; Kahl et al., 2011; Kamenetsky and Clocchiatti, 1996; Métrich and Rutherford, 1998; Trigila et al., 1990), or between NNO and NNO+1 based on S speciation (Métrich and Clocchiatti, 1996; Métrich et al., 2009; Morizet et al., 2017).

In addition to the $Fe^{3+}/\Sigma Fe$ ratio, we applied other methods to estimate the redox conditions for the same group of samples. The oxybarometer method of Arató and Audétat (2017) was used on magnetite-bearing samples to estimate oxygen fugacity from the partitioning of Fe and Ti between magnetite and silicate melt (*FeTiMM*; Table S2 in Supplementary Data Electronic Appendix_2). The calculations suggest ΔNNO from -0.9 to +0.5 for the 2002 MIs, from -0.26 to +0.66 for the 2006 MIs, from -1.47 to +0.85 for the 2008 MIs, and from -1.09 to +0.70 for the 2013 MIs (Fig. 9c, Table S2 in Supplementary Data Electronic Appendix_2).

For four of the magnetite-MI pairs, the XANES $Fe^{3+}/\Sigma Fe$ ratios in the correspondent MI are

known and the fO_2 estimated with the two methods are shown in Figure 9c (and presented in Table S2 in Supplementary Data Electronic Appendix_2).

The oxygen thermo-oxybarometer of Ballhaus et al. (1990) modified by Ballhaus et al. (1991), based on the olivine-spinel equilibrium, was applied only to the Cr-spinel-olivine pairs from Mt. Spagnolo and FS rocks (Table S2 in Supplementary Data Electronic Appendix_2). The calculations yields fO_2 of NNO+1.5±0.1 for both Mt. Spagnolo and FS (Fig. 9c and Table S2), which are in good agreement with those based on the XANES $Fe^{3+}/\Sigma Fe$ ratios. This indicates that post-entrapment modifications have a negligible effect on the $Fe^{3+}/\Sigma Fe$ ratio of the MIs, even when PEC exceeds 10%. More generally, our fO_2 estimations are close to those from previous studies (Fig. 9b), some of which applied to the products of the same eruptions (~NNO to NNO+2; e.g., Armienti et al., 1994; Kahl et al., 2011; Kamenetsky and Clocchiatti, 1996; Métrich and Clocchiatti, 1996; Métrich and Rutherford, 1998; Métrich et al., 2009; Morizet et al., 2017; Trigila et al., 1990). What is evident in Figure 9 is that the determined redox conditions for Etnean product span a very wide range of fO_2, i.e. from NNO-1.5 to NNO+1.8.

DISCUSSION

Differentiation and degassing processes in Etnean magmas

MgO-rich olivine crystals of the FS eruption entrap the most primitive MIs among those of Mt. Etna (e.g., Collins et al., 2009; Corsaro and Métrich, 2016; Gennaro et al., 2019; Kamenetsky and Clocchiatti, 1996; Kamenetsky et al., 2007; Métrich et al., 2004; Moretti et al., 2018; Schiavi et al., 2015; Spilliaert et al., 2006a). These MIs are very rich in volatiles, and their minimum entrapment pressures, retrieved from their H_2O and CO_2 contents using the solubility model of Iacono Marziano et al. (2012), range from 62 to 272 MPa (Table 4). Using a rock density of 2.65 g cm^{-3}, as average for the different lithologies of the crustal

basement (from 2.57 to 2.70 g cm^{-3} in the first 22 km of the crust, as reported in Corsaro and Pompilio, 2004), these pressures correspond to depths varying from 2.4 to 10.5 km below crater level ("bcl"), which are inside the range of previous estimations (4-19 km bcl, e.g., Gennaro et al., 2019; Kamenetsky et al., 2007). Gennaro et al. (2019) proposed that magmas feeding Etnean eruptions in the last 15 ka could have been produced by variable amounts of differentiation of a parental melt with the composition of the most primitive FS MIs ("FS-type magma"), on the basis of differentiation trends observed in MIs and MELTS simulations. Without excluding the occurrence of additional processes (such as mixing events, sulphate assimilation, alkali enrichments, mantle metasomatism or different melting degrees of the mantle source) to thoroughly explain the chemical variability of Etnean magmas, the authors show that MELTS simulations of fractional crystallization of FS-type magma capture most of the first-order features of the Etnean magmas erupted in the last 15 ka (Gennaro et al., 2019). We therefore consider FS most primitive MIs as possible parental melt for the following discussion and modelling.

Variability in Etnean magmatic redox conditions

$Fe^{3+}/\Sigma Fe$ ratios obtained by XANES spectroscopy for Etnean MIs yield a large range of fO_2 values (NNO-1.5 to NNO+1.6 of fO_2) that is corroborated by two independent oxybarometers (magnetite-silicate melt equilibrium, and olivine-spinel equilibrium, see "*Redox conditions of Etnean magmas"* section). These data significantly enlarge the range of previous estimations (~NNO to NNO+2; e.g., Armienti et al., 1994; Kahl et al., 2011; Kamenetsky and Clocchiatti, 1996; Métrich and Clocchiatti, 1996; Métrich and Rutherford, 1998; Métrich et al., 2009; Morizet et al., 2017; Trigila et al., 1990) as shown in Figure 9.

In the following, we will explore two main processes that could explain these variations observed in Etnean magmas: volatile degassing and melt evolution.

Effects of volatile degassing on redox conditions

Several recent studies have discussed the effect of volatile degassing on the variation of the magmatic redox state (e.g., Burgisser and Scaillet, 2007; Gaillard et al., 2011; Moussallam et al., 2014, 2016; Waters and Lange, 2016).

The effect of the degassing of H_2O and CO_2 on the magmatic redox state is controversial, as it is proposed to either oxidize the magma (e.g., Burgisser and Scaillet, 2007; Humphreys et al., 2015; Mathez, 1984), reduce it (e.g., Wilke et al., 2002), or to have no effect on it (Kelley and Cottrell, 2012; Waters and Lange, 2016), depending on melt and fluid phases composition. Indeed, for silicic melt composition, degassing of a H_2O-CO_2 fluid phase is expected to oxidized the melt (e.g., Burgisser and Scaillet, 2007; Humphreys et al., 2015).

In the present case of the Etnean basaltic MIs, no clear correlations is observed between $Fe^{3+}/\Sigma Fe$ ratios and H_2O and CO_2 contents (Figs. 7a-c), while the drop of $Fe^{3+}/\Sigma Fe$ with entrapment pressure from FS toward 2008-2013 MIs (Fig. 8) suggests a reduction of the melt upon decompression and degassing. This, however, does not necessarily mean that H_2O and CO_2 degassing is the cause of the reduction.

Sulphur is known to have an important influence on magmatic redox conditions, due to its varying oxidation states in the silicate melt and in the fluid phase (e.g., Burgisser and Scaillet, 2007; Gaillard and Scaillet, 2009; Gaillard et al., 2011; Métrich et al., 2009; Moussallam et al., 2014, 2016, 2019), and with a difference of 8 electrons between the most oxidized (S^{6+}) and the most reduced form (S^{2-}). The dominant S species measured in the volcanic gases is SO_2, while H_2S and S_2 are minor species (e.g., Oppenheimer, 2003). Even if in recent experimental investigation at low temperature (650–950 °C), H_2S was shown to be the dominant S species at fO_2 between NNO and NNO+0.7 and pressures between 50 and 200 MPa (Binder and Keppler, 2011), SO_2 degassing is increasingly favoured during magma

ascent, since the homogenous equilibrium in gas phase shifts to the left with reducing pressure (Gaillard et al., 2011):

$$SO_2 + 3H_2 = 2H_2O + H_2S \quad [3]$$

According to Métrich et al. (2009), the degassing of SO_2 from an oxidized basaltic Fe-bearing melt, in which the dominant dissolved S species is sulphate [$(SO_4)^{2-}$], causes oxidation of dissolved iron and therefore an increase of Fe^{3+}/Fe^{2+}:

$$CaSO_{4(melt)} + 2Fe^{2+}O_{(melt)} = SO_{2(gas)} + Fe^{3+}{}_2O_{3(melt)} + CaO_{(melt)} \quad [4]$$

Conversely, at more reduced redox conditions, the exsolution of S^{2-} from a Fe-bearing melt induces iron reduction and therefore a decrease of Fe^{3+}/Fe^{2+}:

$$Fe^{2+}S^{2-}{}_{(melt)} + 3Fe^{3+}{}_2O_{3(melt)} = SO_{2(gas)} + 7Fe^{2+}O_{(melt)} \quad [5]$$

Moussallam et al. (2014, 2016) observed a strong reduction of the redox condition of the melt driven by sulphur degassing at Erebus and Kilauea volcanoes, starting from a variable redox conditions (around NNO for Kilauea, and >NNO+1 for Erebus melts).

In order to verify the effect of degassing on the iron speciation ($Fe^{3+}/\Sigma Fe$) of the Etnean magmas, we modelled the degassing of H_2O (the most abundant volatile in magma) and S (the only polyvalent volatile species) using the gas-melt equilibrium models of Gaillard and Scaillet (2009) and Gaillard et al. (2011). Two simulations were performed: one started from a fO_2 of NNO+1.1 (at which S in the melt is preferentially in its oxidized form, SO_4^{2-}), an initial P of 400 MPa, and H_2O and S contents in the melt of 4 wt% and 4000 ppm, respectively; the second simulation started from a fO_2 of NNO+0.5 (at which a more important portion of the S dissolved in the melt is in its reduced form S^{2-}), an initial P of 150 MPa, and H_2O and S contents in the melt of 3 wt% and 1500 ppm, respectively. The temperature (kept constant during the decompression) was of 1200 and 1150 °C, respectively (details of the calculations are in Table S3 in Supplementary Data Electronic Appendix_2). In both simulations, S degassing is indirectly caused by H_2O exsolution from the silicate melt,

which in turn is triggered by decompression. The simulation performed in the most oxidizing redox conditions showed no variations in fO_2 induced by degassing, and generally reproduces the trend presented by FS MIs (green curves in Figs. 7a-b), even if it underestimates their $Fe^{3+}/\Sigma Fe$ ratios. This simulation cannot, however, describe the lower $Fe^{3+}/\Sigma Fe$ ratios shown by 2002-2013 MIs, the embayment and the matrix glass. In contrast, the simulation performed in the most reducing redox conditions (violet curves in Figs. 7a-b) predicts a slight decrease in the $Fe^{3+}/\Sigma Fe$ ratio induced by degassing, without, however, reproducing the whole trend shown by MIs (Figs. 7a-b).

These simulations suggest that the effect of S and H_2O degassing on the $Fe^{3+}/\Sigma Fe$ ratio of the Etnean magma is too small to be the only process controlling the important reduction (from NNO+1.6 to NNO-1.9) recorded by Etnean melt inclusions.

Effects of magma differentiation on redox conditions

The correlation between the $Fe^{3+}/\Sigma Fe$ ratio and several major oxides (Fig. 6) suggests that the variation of the magmatic redox conditions may be related to melt differentiation. For example, the $Fe^{3+}/\Sigma Fe$ ratio of the MIs decreases with decreasing MgO content and CaO/Al_2O_3 ratio, and with increasing SiO_2, K_2O and Na_2O contents (Fig. 6), as previously observed in other magmatic contexts (Kelley and Cottrell, 2012) and in experimental investigations (e.g., Borisov and Mccammon, 2010; Borisov et al., 2015).

We used the MELTS code (Ghiorso and Sack, 1995; Smith and Asimow, 2005) to simulate fractional crystallization in open system conditions upon simultaneous cooling and decompression (at a fixed dP/dT), starting from the most primitive composition of FS MIs (10.5 wt% MgO, 5 wt% of H_2O). In this way, we estimated the evolution of the $Fe^{3+}/\Sigma Fe$ ratio of the residual liquid during the fractional crystallization as calculated by MELTS, and

compared the results with the $Fe^{3+}/\Sigma Fe$ ratio estimated by XANES for the Etnean MIs (FS, Mt. Spagnolo and 2002-2013 eruptions).

The imposed initial T-P values were 1200 °C and 400 MPa, which, together with a dP/dT of 3 MPa $°C^{-1}$, are the conditions that best reproduce the major element variations of the studied MIs according to Gennaro et al. (2019). Oxygen fugacity was allowed to freely evolve during crystallization (i.e. unconstrained). Two initial fO_2 values were used (NNO+1 and NNO+2), in order to bracket the fO_2 estimations for FS MIs (~NNO+1.5, Tables 5 and S2 in Supplementary Data Electronic Appendix_2), considering the high uncertainty likely associated to this estimation (analytical errors, PEC, volatile diffusion, bubbles).

Both simulations predict a decrease of the $Fe^{3+}/\Sigma Fe$ ratio during fractional crystallization (continuous and dashed black curves in Fig. 6), which is dictated by the crystallizing phases (in the simulations only the initial oxygen fugacity is fixed). These variations generally reproduce well the trends shown by MIs, with the exception of the most evolved ones.

The early crystallization of olivine and Mg-Cr-spinel (Cr# = 55-65) at high T and P (1170-1200 °C and 250-400 MPa), calculated by the MELTS code, preferentially transfers Fe^{2+} into the solid phases, inducing a slight increase in the $Fe^{3+}/\Sigma Fe$ ratio in the residual melt, and a slight decrease in total iron, while MgO decreases from 11 wt% to ~9 wt% (Figs. 6b-f). At lower temperatures and pressures, and for the most oxidizing redox conditions simulation, the $Fe^{3+}/\Sigma Fe$ ratio begins to decrease in response to the extensive clinopyroxene crystallization (Fig. 6), which probably consumes more Fe^{3+} than Fe^{2+} (O'Neill et al., 2018). This is accompanied by an increase in total FeO content (continuous black curve in Fig. 6f). A more important decrease in the $Fe^{3+}/\Sigma Fe$ ratio is observed when magnetite starts to crystallize: $Fe^{3+}/\Sigma Fe$ ratios calculated by MELTS simulations decrease to value of ~0.13, which is slightly lower than the lowest $Fe^{3+}/\Sigma Fe$ ratios measured in our MIs (Fig. 6). At higher initial fO_2 (NNO+2), Fe-spinel crystallisation occurs at 1150 °C and ~6 wt% MgO, which sensibly

decreases the FeO_{tot} content of the melt. At lower initial fO_2 (NNO+1), spinel crystallization only occurs at 1085 °C and ~4 wt% MgO, which does not prevent the FeO_{tot} content of the melt to increase up to 10-12 wt%, as observed in 2002, 2006 and 2008/2009 MIs (Figs. 6b-f). Since the MgO and Cr contents of the residual melt decreased, the spinel crystallizing at this stage has a titano-magnetite composition, in agreement with the observations in 2002-2013 eruptive products (e.g., Gennaro et al., 2019; Kahl et al., 2015; Mollo et al., 2015; Schiavi et al., 2015). In contrast, in FS and Mt. Spagnolo olivines, Cr-spinel are detected (e.g., Gennaro et al., 2019; Kamenetsky and Clocchiatti, 1996; Kamenetsky et al., 2007).

MIs from 2013 showed FeO_{tot} contents lower than those predicted by the MELTS models (Fig. 6f), while $Fe^{3+}/\Sigma Fe$ ratio maintains a constant value (~0.21±0.03), which could be due to a more copious crystallization of magnetite (and plagioclase) at constant fO_2 than that predicted by MELTS (Gennaro et al., 2019). This could also explain the lower CaO/Al_2O_3 ratio of these MIs than the values calculated by the liquid line of descent (Fig. 6a). Besides, Figure 6 reveals a discrepancy between alkali contents measured in MIs and those predicted by MELTS (Figs. 6c-d). The alkali contents of 2013 MIs, and to a lower extent those of Mt. Spagnolo and 2002-2008 MIs, are generally higher than those of the liquid line of descent of FS magma, as already noted in Gennaro et al. (2019). Alkali enrichment of the Etnean magmas is highly debated. Among the numerous hypotheses, Correale et al. (2014) proposed that the variability of primitive whole-rock compositions requires variable melting degrees of a single mantle source, followed by crystallization. The enrichment in K_2O has also been attributed to the upward migration of deep Cl-rich fluids carrying alkalis (Ferlito and Lanzafame, 2010), supported by the variable and high Cl concentrations measured in MIs (up to 4600 ppm; e.g., Collins et al., 2009; Gennaro et al., 2019; Moretti et al., 2018). A recent study shows that lowering of water activity during the fractional crystallization of a basaltic

melt yields a decrease in MgO and a significant increase in K_2O relative to SiO_2 contents in the residual liquids (e.g., Beermann et al., 2017).

The good agreement between the estimated $Fe^{3+}/\Sigma Fe$ ratios in MIs and the $Fe^{3+}/\Sigma Fe$ ratio variations (Fig. 6) calculated by the MELTS code for the residual melt during the fractional crystallization of olivine+Mg-Cr-spinel and cpx+Fe-spinel (+plg) suggest that the variation in redox conditions of the Etnean magmas can be significantly affected by melt differentiation via fractional crystallization.

The occurrence of these minerals phases (ol, cpx, plg and Fe-Ti oxides) is common in basalts and trachybasalts erupted by Mt. Etna in the last decades; a variability in redox conditions (between NNO and NNO+2) is likely to influence the percentage and the composition of these minerals (e.g., Armienti et al., 2012; Giacomoni et al., 2016; Kahl et al., 2015; Kamenetsky and Clocchiatti, 1996; Viccaro et al., 2010).

Sulphur behaviour during fractional crystallization of fluid-saturated magmas

Sulphur behaviour in fluid-saturated magmas during crystallization is strictly linked to the proportions of its dissolved species (sulphate and sulphide), as they exhibit different solubilities and are therefore exsolved at different rates: sulphate is more soluble, while sulphide is more volatile and could degas more efficiently (e.g., Carroll and Rutherford, 1985, 1987; Jugo et al., 2005; Luhr, 1990). Oxygen fugacity controls sulphur speciation in both the silicate melt (S^{2-} versus S^{6+}) and the fluid phase (H_2S versus SO_2) and, therefore, affects S degassing behaviour.

In order to model the sulphur behaviour during decompression and crystallization and, therefore, during decreasing of T, P and fO_2 conditions, we calculated the S content of the residual liquid from the results of MELTS crystallization simulations, taking into account the

variation of the experimentally-determined S distribution coefficient between fluid and melt ($DS^{fluid/melt}$; see *"S content in the fluid phase and fluid/melt partitioning"* section).

Although associated with large uncertainties, the constructed empirical model provides a suitable approach to estimate $DS^{fluid/melt}$ value in basaltic magmas as a function of the three intensive variables (T, P and fO_2).

We used (i) the crystallization simulation performed in T-P-fO_2 range of 1200-1068 °C, 400-0.1 MPa, NNO+2 to NNO-1.8 using MELTS code and a fixed dP/dT ratio of 3 MPa $°C^{-1}$, which well reproduces the chemical trends shown by the MIs (Fig. 6), and (ii) an additional MELTS simulation performed in the same T-P-fO_2 range with a dP/dT ratio of 20 MPa $°C^{-1}$, which better reproduces the highest decompression rate experienced by FS magma (Gennaro et al. 2019). Each step of MELTS simulations returns the composition of the residual liquids after crystallization due to the ΔP-ΔT change corresponding to the considered dP/dT ratio. For each step, the sulphur content of the residual melt (S_{MELTS}) is then calculated using the following equation:

$$S_{MELTS} = (S^*_{MELTS} \cdot M_{syst}) / (M_{melt} + M_{fluid} \cdot DS^{fluid/melt}) \quad [6]$$

in which M_{syst}, M_{melt} and M_{fluid} are respectively the masses of the total system, the residual melt and the fluid phase and S^*_{MELTS} is the S content of the previous step in the MELTS simulation. As initial S^*_{MELTS} we used the maximum S content in the FS MIs (S=3445 ppm, Table 4). M_{syst}, and M_{melt} are calculated by MELTS code, while the mass of the fluid phase (M_{fluid}) is calculated in each step of MELTS simulation (n, n+1, n+2, …), as following:

$$M_{fluid\,(n+1)} = (M_{melt} \cdot H_2O_{MELTS\,(n)}/\,100)_n - (M_{melt} \cdot H_2O_{MELTS\,(n+1)}/\,100)_{(n+1)} \quad [7]$$

where H_2O_{MELTS} is the H_2O content in the residual melt, calculated by MELTS code, at each step of fractional crystallization.

The S content obtained using equations *[6-7]* is shown in Figs. 10 and 11 as a function of the MgO and K_2O contents of the melt, both being markers of melt differentiation, and of fO_2 variation.

The simulation using a dP/dT of 20 MPa $°C^{-1}$ (red curve in Figs. 10a-b and 11), describes a rapid decompression with a low fractional crystallization, and is accompanied by a slight decrease of fO_2 (from NNO+2 to NNO+1.5) and a continuous decrease of S content in the melt. The important S degassing is favoured by the significant pressure decrease, accompanied by H_2O exsolution, as also predicted by S-H_2O degassing simulations (Figs. 7a-b). The amount of S degassing simulated following this dP/dT rate (red curves in Figs. 10 and 11) is analogous to that observed in FS MIs, which is accompanied by a decrease in fO_2 from NNO+1.6 to NNO+0.7 (Table 5). Based on this evidence, FS eruption is probably unique in the eruptive history of Etna and was most likely produced by an unusually strong and rapid decompression of the magma, inducing explosive CO_2-H_2O and S degassing.

In contrast, the simulation performed using a dP/dT of 3 MPa $°C^{-1}$ (blue curve in Figs. 10a-b and 11) is characterized by major crystallization and subsequent fO_2 reduction (from NNO+2 to NNO-1.8). The S content of the melt slightly decreases during the early crystallization (of ol+Fe-oxide), when fO_2 is around NNO+1.9 and the MgO content is higher than 9 wt% (Figs. 6b, 10a and 11). At these conditions, neither decompression nor crystallization are effective for sulphate degassing.

When cpx starts to crystallize in major quantity, S initially slightly increases and then resumes decreasing. At a more advanced melt evolution (MgO content lower than 6 wt%, Fig. 10a), MELTS code calculates a decrease in fO_2 from NNO+1.3 to NNO-1.7, as a consequence of fractional crystallization of cpx+ Fe-Ti-spinel (and at final step, plg), which leads to an important S decrease in the silicate melt (Fig. 11). This trend is observed in 2002-2013 (and partially in Mt. Spagnolo) MIs, which are characterized by a decrease in $Fe^{3+}/\Sigma Fe$ ratio from

0.25 to 0.17, corresponding to a decrease in fO_2 from NNO+1 to NNO-1.5 (Figs. 6, 7, 11, Tables 5 and S2 in Supplementary Data Electronic Appendix_2). Therefore, while crystallization induces S-enrichment in the melt, the conversion of sulphate to scarcely soluble sulphide causes extensive degassing and a drastic drop of the S content in the melt (down to <100 ppm at $\log fO_2 <$ NNO, Fig. 11).

The variability shown by the MIs of the same eruption could reflect the effects of other volatiles, like CO_2 and Cl, on S degassing. These volatiles are not accounted for by the presented $DS^{fluid/melt}$ calibration model, and could influence the $DS^{fluid/melt}$ (e.g., Beermann et al., 2015; Fiege et al., 2015).

In conclusion, as suggested by our and previous (e.g., Beermann et al., 2011, 2015; Fiege et al., 2015; Lesne et al., 2011b) experimental results, oxygen fugacity probably exerts the major control on the S content of Etnean melts, and ensures efficient S degassing during magma ascent.

Most of the MIs presented in Figures 10 and 11 do not contain sulphide globules, which were observed only in a few evolved and degassed MIs estimated to be entrapped at $fO_2 <$ NNO-0.2 (from 2006, 2008/2009 and 2013 products; Gennaro et al., 2019). More generally, sulphide globules are rare in Etnean MIs and matrix glasses, and they always occur in evolved and degassed glasses (Collins et al., 2009; Gennaro et al., 2019; Spilliaert et al., 2006a, 2006b). This rules out the segregation of important amounts of immiscible sulphide melt, despite the reduction experienced by the magma during crystallization. At fluid-saturated conditions, the most important effect of magma reduction is therefore to enhance S degassing, as sulphide species are significantly less soluble in the silicate melt than sulphate ones (Fig. 2a). Reduction-induced degassing is probably a more efficient mechanism than (i) a simple crystallization-driven degassing or (ii) decompression, considering that the effect of fO_2 significantly enhances that of P in increasing the $DS^{fluid/melt}$ (Fig. 3). This process is therefore

likely to account for the significant gas emissions observed at Mt. Etna (e.g., Aiuppa et al., 2005, 2008; D'Aleo et al., 2016; Delle Donne et al., 2019; McGonigle et al., 2003; Salerno et al., 2009).

CONCLUSIONS

S behaviour in basaltic magmas of Mt. Etna (Italy) has been investigated by means of olivine-hosted melt inclusions and an experimental approach. The experimental study of S solubility in a hydrous basaltic melt from Mt. Etna (Mt. Spagnolo eruption) was performed at constant temperature and pressure (1200 °C and 200 MPa) and variable oxygen fugacity (NNO+0.2 to NNO+1.7). In addition to former studies, our results confirm the dependence of $DS^{fluid/melt}$ of the hydrous basaltic melt on the redox conditions, displaying a sulphur concentration of 6039±232 ppm at NNO+1.7±0.5 with a $DS^{fluid/melt}$ of 51±4.

Based on a selection of the obtained experimental $DS^{fluid/melt}$ values (50-146) and of those of literature (1-209; e.g., Beermann et al., 2015; Le Gall, 2015; Lesne et al., 2011b; Zajacz et al., 2013), an empirical model is proposed for basaltic melt composition in order to predict the variation of $DS^{fluid/melt}$ values upon variation of P, T and fO_2 conditions (25-300 MPa, 1030-1200 °C and between NNO-0.8 and NNO+2.4). This empirical model is applied to Mt. Etna basaltic magmas, for which fO_2 conditions are here for the first time directly defined in olivine-hosted melt inclusions using XANES $Fe^{3+}/\Sigma Fe$ ratios.

Fe speciation in Etnean melt inclusions, together with olivine-spinel exchange (Ballhaus et al., 1990, 1991) in the same products, reveal that the most primitive FS (4 ka BP) and Mt. Spagnolo (4-15 ka BP) magmas are highly oxidized (up to NNO+1.6). The more evolved products from 2002-2013 eruptions indicate more reduced redox conditions, based on XANES $Fe^{3+}/\Sigma Fe$ ratios (NNO-0.9 to NNO+0.4) and Fe-Ti-spinel equilibria (NNO-1.4 to

NNO+0.9). The S content of these Etnean MIs is extremely variable, from ~100 ppm to more than 4000 ppm.

Crystal fractionation and degassing models suggest that fractional crystallization coupled with magma degassing is the driving process accounting for both the variability in sulphur content and the large fO_2 variations observed in Etnean MIs.

The $DS^{fluid/melt}$ model coupled to the MELTS code (Ghiorso and Sack, 1995; Smith and Asimow, 2005) reveals that upon decrease of T and P, during fractional crystallization of ol+sp+cpx+plg (and volatile exsolution) of a FS-type magma, a significant fO_2 diminution occurs. The fO_2 reduction, in turn, causes a decrease in sulphur solubility and an increase in $DS^{fluid/melt}$. This increase becomes particularly important at $fO_2 \leq$ NNO+1, when S is preferentially dissolved in the melt as S^{2-} (e.g., Carroll and Rutherford, 1985, 1987; Jugo et al., 2005; Luhr, 1990), and $DS^{fluid/melt}$ is higher than 90, suggesting that S partitions favourably in the fluid phase.

Thus, important S degassing, as observed in the last decades at Mt. Etna (Aiuppa et al., 2005, 2008; D'Aleo et al., 2016; Delle Donne et al., 2019; McGonigle et al., 2003; Salerno et al., 2009), could highlight the ascent of magma batches, subjected to variation in fO_2 conditions associated to melt evolution.

FUNDING

This research has been financially supported by the *Università degli Studi di Palermo*, the *Agence Campus France,* the MEDiterranean SUpersite Volcanoes (MED-SUV) project, the "*Laboratoire d'Excellence VOLTAIRE" de l'Université d'Orléans,* and the French *Agence Nationale de la Recherche* (ANR project #12-JS06-0009-01).

ACKNOWLEDGMENTS

We are grateful to I. Di Carlo (ISTO, Orléans) for her assistance with the SEM and the EMP, to E. Deloule, J. Villeneuve and A. Gurenko (CRPG, Nancy) for their support during SIMS acquisitions. XANES analyses were carried out at the Diamond Light Source using beamline I18 (proposal number SP17250-1) with invaluable support received from K. Ignatyev.
We thank A. Rizzo, A. Correale, M. Liotta and S. Rotolo (INGV, Palermo) to have provided the Etnean samples, and for the precious discussions.
We wish to thank O. Beermann, M. Masotta, two anonymous reviewers and the editor A. Audétat for their constructive reviews and useful comments.

REFERENCES

Aiuppa, A., Inguaggiato, S., McGonigle, A.J.S., O'dwyer, M., Oppenheimer, C., Padgett, M.J., Rouwet, D., Valenza, M., 2005. H_2S fluxes from Mt. Etna, Stromboli, and Vulcano (Italy) and implications for the sulfur budget at volcanoes. Geochimica et Cosmochimica Acta 69, 1861–1871.

Aiuppa, A., Giudice, G., Gurrieri, S., Liuzzo, M., Burton, M., Caltabiano, T., McGonigle, A.J.S., Salerno, G., Shinohara, H., Valenza, M., 2008. Total volatile flux from Mount Etna. Geophysical Research Letters 35, L24302. https://doi.org/10.1029/2008GL035871

Allard, P., Behncke, B., D'Amico, S., Neri, M., Gambino, S., 2006. Mount Etna 1993–2005: Anatomy of an evolving eruptive cycle. Earth-Science Reviews 78, 85–114. https://doi.org/10.1016/j.earscirev.2006.04.002

Alletti, M., Baker, D.R., Scaillet, B., Aiuppa, A., Moretti, R., Ottolini, L., 2009. Chlorine partitioning between a basaltic melt and H_2O–CO_2 fluids at Mount Etna. Chemical Geology, Halogens in Volcanic Systems and Their Environmental Impacts 263, 37–50. https://doi.org/10.1016/j.chemgeo.2009.04.003

Arató, R., Audétat, A., 2017. FeTiMM – A new oxybarometer for mafic to felsic magmas. Geochemical Perspectives Letters 5, 19–23. https://doi.org/10.7185/geochemlet.1740

Armienti, P., Innocenti, F., Petrini, R., Pompilio, M., Villari, L., 1988. Sub-aphyric alkali basalt from Mt. Etna: inferences on the depth and composition of the source magma. Rendiconti Società Italiana di Mineralogia e Petrologia 43, 877–891.

Armienti, P., Pareschi, M.T., Innocenti, F., Pompilio, M., 1994. Effects of magma storage and ascent on the kinetics of crystal growth. Contributions to Mineralogy and Petrology 115, 402–414.

Armienti, P., Tonarini, S., D'Orazio, M., Innocenti, F., 2004. Genesis and evolution of Mt. Etna alkaline lavas: Petrological and Sr-Nd-B isotope constraints. Periodico di Mineralogia 73, 29–52.

Armienti, P., Perinelli, C., Putirka, K.D., 2012. A New Model to Estimate Deep-level Magma Ascent Rates, with Applications to Mt. Etna (Sicily, Italy). Journal of Petrology 54, 795–813. https://doi.org/10.1093/petrology/egs085

Ballhaus, C., Berry, R.F., Green, D.H., 1990. Oxygen fugacity controls in the Earth's upper mantle. Nature 348, 437. https://doi.org/10.1038/348437a0

Ballhaus, C., Berry, R.F., Green, D.H., 1991. High pressure experimental calibration of the olivine-orthopyroxene-spinel oxygen geobarometer: implications for the oxidation state of the upper mantle. Contributions to Mineralogy and Petrology 107, 27–40. https://doi.org/10.1007/BF00311183

Ballhaus, C., 1993. Redox states of lithospheric and asthenospheric upper mantle. Contributions to Mineralogy and Petrology 114, 331–348. https://doi.org/10.1007/BF01046536

Beermann, O., Botcharnikov, R., Holtz, F., Diedrich, O., Nowak, M., 2011. Temperature dependence of sulfide and sulfate solubility in olivine-saturated basaltic magmas.

Geochimica et Cosmochimica Acta - 75, 7612–7631. https://doi.org/10.1016/j.gca.2011.09.024

Beermann, O., Botcharnikov, R.E., Nowak, M., 2015. Partitioning of sulfur and chlorine between aqueous fluid and basaltic melt at 1050 °C, 100 and 200 MPa. Chemical Geology 418, 132–157. https://doi.org/10.1016/j.chemgeo.2015.08.008

Beermann, O., Holtz, F., Duesterhoeft, E., 2017. Magma storage conditions and differentiation of the mafic Lower Pollara volcanics, Salina Island, Aeolian Islands, Italy: implications for the formation conditions of shoshonites and potassic rocks. Contributions to Mineralogy and Petrology 172, 37. https://doi.org/10.1007/s00410-017-1363-z

Binder, B., Keppler, H., 2011. The oxidation state of sulfur in magmatic fluids. Earth and Planetary Science Letters 301, 190–198. https://doi.org/10.1016/j.epsl.2010.10.042

Binder, B., Wenzel, T., Keppler, H., 2018. The partitioning of sulfur between multicomponent aqueous fluids and felsic melts. Contributions to Mineralogy and Petrology 173. https://doi.org/10.1007/s00410-018-1445-6

Borisov, A., Mccammon, C., 2010. The effect of silica on ferric/ferrous ratio in silicate melts: An experimental study using Mossbauer spectroscopy. American Mineralogist 95, 545–555. https://doi.org/10.2138/am.2010.3217

Borisov, A., Behrens, H., Holtz, F., 2015. Effects of melt composition on Fe^{3+}/Fe^{2+} in silicate melts: a step to model ferric/ferrous ratio in multicomponent systems. Contributions to Mineralogy and Petrology 169, 24. https://doi.org/10.1007/s00410-015-1119-6

Botcharnikov, R.E., Behrens, H., Holtz, F., Koepke, J., Sato, H., 2004. Sulfur and chlorine solubility in Mt. Unzen rhyodacitic melt at 850 °C and 200 MPa. Chemical Geology, 7th Silicate Melt Workshop 213, 207–225. https://doi.org/10.1016/j.chemgeo.2004.08.044

Botcharnikov, R.E., Linnen, R.L., Wilke, M., Holtz, F., Jugo, P.J., Berndt, J., 2011. High gold concentrations in sulphide-bearing magma under oxidizing conditions. Nature Geoscience 4, 112.

Bourgue, E., Richet, P., 2001. The effects of dissolved CO_2 on the density and viscosity of silicate melts: A preliminary study. Earth and Planetary Science Letters 193, 57–68. https://doi.org/10.1016/S0012-821X(01)00491-5

Branca, S., Coltelli, M., Groppelli, G., 2011. Geological evolution of a complex basaltic stratovolcano: Mount Etna, Italy. Italian Journal of Geosciences 130 (3), 306-317. https://doi.org/10.3301/IJG.2011.13

Brugier, Y.-A., Alletti, M., Pichavant, M., 2015. Fe pre-enrichment: A new method to counteract iron loss in experiments on basaltic melts. American Mineralogist 100, 2106–2111. https://doi.org/10.2138/am-2015-5166

Bucholz, C.E., Gaetani, G.A., Behn, M.D., Shimizu, N., 2013. Post-entrapment modification of volatiles and oxygen fugacity in olivine-hosted melt inclusions. Earth and Planetary Science Letters 374, 145–155. https://doi.org/10.1016/j.epsl.2013.05.033

Burgisser, A., Scaillet, B., 2007. Redox evolution of a degassing magma rising to the surface. Nature 445, 194–197. https://doi.org/10.1038/nature05509

Burnham, W. C., 1979. The importance of volatile constituents. In: Yoder, H. S., Jr (ed.) The Evolution of Igneous Rocks. Princeton University Press, pp. 439-482.

Carroll, M.R., Rutherford, M.J., 1985. Sulfide and sulfate saturation in hydrous silicate melts. Journal of Geophysical Research Solid Earth 90, C601–C612. https://doi.org/10.1029/JB090iS02p0C601

Carroll, M.R., Rutherford, M.J., 1987. The Stability of Igneous Anhydrite: Experimental Results and Implications for Sulfur Behavior in the 1982 El Chichon Trachyandesite

and Other Evolved Magmas. Journal of Petrology 28, 781–801. https://doi.org/10.1093/petrology/28.5.781

Carroll, M., Rutherford, M., 1988. Sulfur speciation in hydrous experimental glasses of varying oxidation-state—Results from measured wavelength shifts of sulfur X-Rays. American Mineralogist 73, 845–849.

Carroll, M., Webster, J.D., 1994. Solubilities of sulfur, noble gases, nitrogen, chlorine and fluorine in magmas. Volatiles in Magmas 30.

Cecchetti A., Marianelli P. and Sbrana A., 2002. L'eruzione Di Astroni (Caldera Dei Campi Flegrei): Dati Preliminari Dallo Studio Di Inclusioni Silicatiche. Atti della Società toscana di scienze naturali. Memorie, Serie A, 108 (2002-2003) paggine. 59-63.

Clemente, B., Scaillet, B., Pichavant, M., 2004. The Solubility of Sulphur in Hydrous Rhyolitic Melts. Journal of Petrology 45, 2171–2196. https://doi.org/10.1093/petrology/egh052

Clocchiatti, R., Schiano, P., Ottolini, L., Bottazzi, P., 1998. Earlier alkaline and transitional magmatic pulsation of Mt Etna volcano. Earth Planetary Science Letters 163, 399–407. https://doi.org/10.1016/S0012-821X(98)00170-8

Cole-Dai, J., Ferris, D., Lanciki, A., Savarino, J., Baroni, M., Thiemens, M.H., 2009. Cold decade (AD 1810–1819) caused by Tambora (1815) and another (1809) stratospheric volcanic eruption. Geophysical Research Letters 36. https://doi.org/10.1029/2009GL040882

Collins, S.J., Pyle, D.M., Maclennan, J., 2009. Melt inclusions track pre-eruption storage and dehydration of magmas at Etna. Geology 37, 571–574. https://doi.org/10.1130/G30040A.1

Coltelli, M., Del Carlo, P., Pompilio, M., Vezzoli, L., 2005. Explosive eruption of a picrite: The 3930 BP subplinian eruption of Etna volcano (Italy). Geophysical Research Letters 32, L23307. https://doi.org/10.1029/2005GL024271

Correale, A., Paonita, A., Martelli, M., Rizzo, A., Rotolo, S.G., Corsaro, R.A., Di Renzo, V., 2014. A two-component mantle source feeding Mt. Etna magmatism: Insights from the geochemistry of primitive magmas. Lithos 184, 243–258. https://doi.org/10.1016/j.lithos.2013.10.038

Corsaro, R.A., Pompilio, M., 2004. Buoyancy-controlled eruption of magmas at Mt Etna. Terra Nova 16, 16–22. https://doi.org/10.1046/j.1365-3121.2003.00520.x

Corsaro, R.A., Métrich, N., Allard, P., Andronico, D., Miraglia, L., Fourmentraux, C., 2009. The 1974 flank eruption of Mount Etna: An archetype for deep dike-fed eruptions at basaltic volcanoes and a milestone in Etna's recent history. Journal of Geophysical Research Solid Earth 114, B07204. https://doi.org/10.1029/2008JB006013

Corsaro, R.A., Métrich, N., 2016. Chemical heterogeneity of Mt. Etna magmas in the last 15 ka. Inferences on their mantle sources. Lithos 252, 123–134. https://doi.org/10.1016/j.lithos.2016.02.006

Cottrell, E., Kelley, K.A., 2011. The oxidation state of Fe in MORB glasses and the oxygen fugacity of the upper mantle. Earth and Planetary Science Letters 305, 270–282. https://doi.org/10.1016/j.epsl.2011.03.014

Cottrell, E., Kelley, K.A., Lanzirotti, A., Fischer, R.A., 2009. High-precision determination of iron oxidation state in silicate glasses using XANES. Chemical Geology 268, 167–179. https://doi.org/10.1016/j.chemgeo.2009.08.008

D'Aleo, R., Bitetto, M., Delle Donne, D., Tamburello, G., Battaglia, A., Coltelli, M., Patanè, D., Prestifilippo, M., Sciotto, M., Aiuppa, A., 2016. Spatially resolved SO_2 flux

emissions from Mt Etna. Geophysical Research Letters 43, 2016GL069938. https://doi.org/10.1002/2016GL069938

Danyushevsky, L.V., McNeill, A.W., Sobolev, A.V., 2002. Experimental and petrological studies of melt inclusions in phenocrysts from mantle-derived magmas: an overview of techniques, advantages and complications. Chemical Geology, Melt Inclusions at the Millennium: Toward a Deeper Understanding of Magmatic Processes 183, 5–24. https://doi.org/10.1016/S0009-2541(01)00369-2

Danyushevsky, L.V., Plechov, P., 2011. Petrolog3: Integrated software for modeling crystallization processes. Geochemistry, Geophysics, Geosystems 12, Q07021. https://doi.org/10.1029/2011GC003516

Delle Donne, D., Aiuppa, A., Bitetto, M., D'Aleo, R., Coltelli, M., Coppola, D., Pecora, E., Ripepe, M., Tamburello, G., 2019. Changes in SO_2 Flux Regime at Mt. Etna Captured by Automatically Processed Ultraviolet Camera Data. Remote Sensing 11, 1201. https://doi.org/10.3390/rs11101201

Di Carlo, I., Pichavant, M., Rotolo, S.G., Scaillet, B., 2006. Experimental Crystallization of a High-K Arc Basalt: the Golden Pumice, Stromboli Volcano (Italy). Journal of Petrology 47, 1317–1343. https://doi.org/10.1093/petrology/egl011

Di Renzo, V., Corsaro, R.A., Miraglia, L., Pompilio, M., Civetta, L., 2019. Long and short-term magma differentiation at Mt. Etna as revealed by Sr-Nd isotopes and geochemical data. Earth-Science Reviews 190, 112–130. https://doi.org/10.1016/j.earscirev.2018.12.008

Dixon, J.E., Stolper, E., Delaney, J.R., 1988. Infrared spectroscopic measurements of CO_2 and H_2O in Juan de Fuca Ridge basaltic glasses. Earth and Planetary Science Letters 90, 87–104. https://doi.org/10.1016/0012-821X(88)90114-8

Dixon, J.E., Pan, V., 1995. Determination of the molar absorptivity of dissolved carbonate in basanitic glass. American Mineralogist 80, 1339–1342.

Ferlito, C., Lanzafame, G., 2010. The role of supercritical fluids in the potassium enrichment of magmas at Mount Etna volcano (Italy). Lithos 119, 642–650.

Fiege, A., Holtz, F., Behrens, H., Mandeville, C.W., Shimizu, N., Crede, L.S., Göttlicher, J., 2015. Experimental investigation of the S and S-isotope distribution between H_2O–S±Cl fluids and basaltic melts during decompression. Chemical Geology 393–394, 36–54. https://doi.org/10.1016/j.chemgeo.2014.11.012

Fincham C. J. B., Richardson Frederick Denys, Goodeve Charles Frederick, 1954. The behaviour of sulphur in silicate and aluminate melts. Proceedings of the Royal Society of London. Series A. Mathematical and Physical Sciences 223, 40–62. https://doi.org/10.1098/rspa.1954.0099

Fortin, M.-A., Riddle, J., Desjardins-Langlais, Y., Baker, D.R., 2015. The effect of water on the sulfur concentration at sulfide saturation (SCSS) in natural melts. Geochimica et Cosmochimica Acta 160, 100–116. https://doi.org/10.1016/j.gca.2015.03.022

Frezzotti, M.-L., 2001. Silicate-melt inclusions in magmatic rocks: applications to petrology. Lithos 55, 273–299. https://doi.org/10.1016/S0024-4937(00)00048-7

Frost, B.R., 1991. Introduction to oxygen fugacity and its petrologic importance. Reviews in Mineralogy and Geochemistry 25, 1–9.

Gaetani, G.A., Watson, E.B., 2000. Open system behavior of olivine-hosted melt inclusions. Earth and Planetary Science Letters 183, 27–41. https://doi.org/10.1016/S0012-821X(00)00260-0

Gaillard, F., Scaillet, B., 2009. The sulfur content of volcanic gases on Mars. Earth and Planetary Science Letters 279, 34–43. https://doi.org/10.1016/j.epsl.2008.12.028

Gaillard, F., Scaillet, B., Arndt, N.T., 2011. Atmospheric oxygenation caused by a change in volcanic degassing pressure. Nature 478, 229–232. https://doi.org/10.1038/nature10460

Gennaro, M.E., 2017. Sulfur behavior and redox conditions in Etnean hydrous basalts inferred from melt inclusions and experimental glasses. Univ. d'Orléans (France) and Univ. di Palermo (Italy).

Gennaro, E., Iacono-Marziano, G., Paonita, A., Rotolo, S.G., Martel, C., Rizzo, A.L., Pichavant, M., Liotta, M., 2019. Melt inclusions track melt evolution and degassing of Etnean magmas in the last 15 ka. Lithos 324–325, 716–732. https://doi.org/10.1016/j.lithos.2018.11.023

Ghiorso, M.S., Sack, R.O., 1995. Chemical mass transfer in magmatic processes IV. A revised and internally consistent thermodynamic model for the interpolation and extrapolation of liquid-solid equilibria in magmatic systems at elevated temperatures and pressures. Contributions to Mineralogy and Petrology 119, 197–212. https://doi.org/10.1007/BF00307281

Giacomoni, P.P., Coltorti, M., Bryce, J.G., Fahnestock, M.F., Guitreau, M., 2016. Mt. Etna plumbing system revealed by combined textural, compositional, and thermobarometric studies in clinopyroxenes. Contributions to Mineralogy and Petrology 171, 34. https://doi.org/10.1007/s00410-016-1247-7

Guo, S., Bluth, G.J.S., Rose, W.I., Watson, I.M., Prata, A.J., 2004. Re-evaluation of SO_2 release of the 15 June 1991 Pinatubo eruption using ultraviolet and infrared satellite sensors. Geochemistry, Geophysics, Geosystems 5. https://doi.org/10.1029/2003GC000654

Hartley, M.E., Shorttle, O., Maclennan, J., Moussallam, Y., Edmonds, M., 2017. Olivine-hosted melt inclusions as an archive of redox heterogeneity in magmatic systems.

Earth and Planetary Science Letters 479, 192–205. https://doi.org/10.1016/j.epsl.2017.09.029

Holloway, J.R., 1987. Igneous fluids. Reviews in Mineralogy and Geochemistry 17, 211–233.

Humphreys, M.C.S., Brooker, R.A., Fraser, D.G., Burgisser, A., Mangan, M.T., McCammon, C., 2015. Coupled interactions between volatile activity and Fe oxidation state during arc crustal processes. Journal of Petrology 56, 795–814. https://doi.org/http://dx.doi.org/10.1093/petrology/egv017

Iacono Marziano, G., Morizet, Y., Le Trong, E., Gaillard, F., 2012. New experimental data and semi-empirical parameterization of H_2O-CO_2 solubility in mafic melts. Geochimica et Cosmochimica Acta 97, 1–23. https://doi.org/10.1016/j.gca.2012.08.035

Jochum, K.P., Stoll, B., Herwig, K., Willbold, M., Hofmiann, A.W., Amini, M., Aarburg, S., Abouchami, W., Hellebrand, E., Mocek, B., Raczek, I., Stracke, A., Alard, O., Bouman, C., Becker, S., Dücking, M., Brätz, H., Klemd, R., Bruin, D.D., Canil, D., Cornell, D., Hoog, C.J.D., Dalpé, C., Danyushevshy, L., Eisenhauer, A., Gao, Y., Snow, J.E., Groschopf, N., Günther, D., Latkoczy, C., Guillong, M., Hauri, E.H., Höfer, H.E., Lahaye, Y., Horz, K., Jacob, D.E., Kasemann, S.A., Kent, A.J.R., Ludwig, T., Zack, T., Mason, P.R.D., Meixner, A., Rosner, M., Misawa, K., Nash, B.P., Pfänder, J., Premo, W.R., Sun, W.D., Tiepolo, M., Vannucci, R., Vennemann, T., Wayne, D., Woodhead, J.D., 2006. MPI-DING reference glasses for in situ microanalysis: New reference values for element concentrations and isotope ratios. Geochemistry, Geophysics, Geosystems 7, 1–44. https://doi.org/10.1029/2005GC001060

Jugo, P.J., Luth, R.W., Richards, J.P., 2005. An experimental study of the sulfur content in basaltic melts saturated with immiscible sulfide or sulfate liquids at 1300° C and 1· 0 GPa. Journal of Petrology 46, 783–798.

Jugo, P.J., 2009. Sulfur content at sulfide saturation in oxidized magmas. Geology 37, 415–418. https://doi.org/10.1130/G25527A.1

Kahl, M., Chakraborty, S., Costa, F., Pompilio, M., 2011. Dynamic plumbing system beneath volcanoes revealed by kinetic modeling, and the connection to monitoring data: An example from Mt. Etna. Earth and Planetary Science Letters 308, 11–22. https://doi.org/10.1016/j.epsl.2011.05.008

Kahl, M., Chakraborty, S., Pompilio, M., Costa, F., 2015. Constraints on the Nature and Evolution of the Magma Plumbing System of Mt. Etna Volcano (1991–2008) from a Combined Thermodynamic and Kinetic Modelling of the Compositional Record of Minerals. Journal of Petrology 56, 2025–2068. https://doi.org/10.1093/petrology/egv063

Kamenetsky, V., Clocchiatti, R., 1996. Primitive magmatism of Mt. Etna: insights from mineralogy and melt inclusions. Earth and Planetary Science Letters 142, 553–572. https://doi.org/10.1016/0012-821X(96)00115-X

Kamenetsky, V.S., Pompilio, M., Métrich, N., Sobolev, A.V., Kuzmin, D.V., Thomas, R., 2007. Arrival of extremely volatile-rich high-Mg magmas changes explosivity of Mount Etna. Geology 35, 255–258. https://doi.org/10.1130/G23163A.1

Kelley, K.A., Cottrell, E., 2012. The influence of magmatic differentiation on the oxidation state of Fe in a basaltic arc magma. Earth and Planetary Science Letters 329–330, 109–121. https://doi.org/10.1016/j.epsl.2012.02.010

Kress, V.C., Carmichael, I.S.E., 1991. The compressibility of silicate liquids containing Fe_2O_3 and the effect of composition, temperature, oxygen fugacity and pressure on their

redox states. Contributions to Mineralogy and Petrology 108, 82–92. https://doi.org/10.1007/BF00307328

Le Gall, N., 2015. Ascension et dégazage des magmas basaltiques : approche expérimentale. Université d'Orléans.

Lesne, P., 2008. Etude expérimentale de la solubilité des volatils C-H-O-S dans les basaltes alcalins italiens. Simulations numériques du dégazage chimique : application à l'Etna. Université d'Orléans.

Lesne, P., Bruno Scaillet, Michel Pichavant, Jean-Michel Bény, 2011a. The carbon dioxide solubility in alkali basalts: an experimental study. Contributions to Mineralogy and Petrology 162, 153–168. https://doi.org/10.1007/s00410-010-0585-0

Lesne, P., Kohn, S.C., Blundy, J., Witham, F., Botcharnikov, R.E., Behrens, H., 2011b. Experimental Simulation of Closed-System Degassing in the System Basalt–H_2O–CO_2–S–Cl. Journal of Petrology 52, 1737–1762. https://doi.org/10.1093/petrology/egr027

Lesne, P., Scaillet, B., Pichavant, M., 2015. The solubility of sulfur in hydrous basaltic melts. Chemical Geology 418, 104–116. https://doi.org/10.1016/j.chemgeo.2015.03.025

Li, C., Ripley, E.M., 2009. Sulfur Contents at Sulfide-Liquid or Anhydrite Saturation in Silicate Melts: Empirical Equations and Example Applications. Economic Geology 104, 405–412. https://doi.org/10.2113/gsecongeo.104.3.405

Liu, Y., Samaha, N.-T., Baker, D.R., 2007. Sulfur concentration at sulfide saturation (SCSS) in magmatic silicate melts. Geochimica et Cosmochimica Acta 71, 1783–1799. https://doi.org/10.1016/j.gca.2007.01.004

Luhr, J.F., 1990. Experimental Phase Relations of Water- and Sulfur-Saturated Arc Magmas and the 1982 Eruptions of El Chichón Volcano. Journal of Petrology 31, 1071–1114. https://doi.org/10.1093/petrology/31.5.1071

Masotta, M., Keppler, H., 2015. Anhydrite solubility in differentiated arc magmas. Geochimica et Cosmochimica Acta 158, 79–102. https://doi.org/10.1016/j.gca.2015.02.033

Masotta, M., Keppler, H., Chaudhari, A., 2016. Fluid-melt partitioning of sulfur in differentiated arc magmas and the sulfur yield of explosive volcanic eruptions. Geochimica et Cosmochimica Acta 176, 26–43. https://doi.org/10.1016/j.gca.2015.12.014

Mathez, E.A., 1984. Influence of degassing on oxidation states of basaltic magmas. Nature 310, 371–375. https://doi.org/10.1038/310371a0

McGonigle, A.J.S., Oppenheimer, C., Hayes, A.R., Galle, B., Edmonds, M., Caltabiano, T., Salerno, G., Burton, M., Mather, T.A., 2003. Sulphur dioxide fluxes from Mount Etna, Vulcano, and Stromboli measured with an automated scanning ultraviolet spectrometer. Journal of Geophysical Research Solid Earth 108, 2455. https://doi.org/10.1029/2002JB002261

Métrich, N., Clocchiatti, R., 1989. Melt inclusion investigation of the volatile behaviour in historic alkali basaltic magmas of Etna. Bulletin of Volcanology 51, 185–198. https://doi.org/10.1007/BF01067955

Métrich, N., Clocchiatti, R., 1996. Sulfur abundance and its speciation in oxidized alkaline melts. Geochimica et Cosmochimica Acta 60, 4151–4160. https://doi.org/10.1016/S0016-7037(96)00229-3

Métrich, N., Rutherford, M.J., 1998. Low Pressure Crystallization Paths of H_2O-Saturated Basaltic-Hawaiitic Melts from Mt Etna: Implications for Open-System Degassing of Basaltic Volcanoes. Geochimica et Cosmochimica Acta 62, 1195–1205. https://doi.org/10.1016/S0016-7037(98)00048-9

Métrich, N., Allard, P., Spilliaert, N., Andronico, D., Burton, M., 2004. 2001 flank eruption of the alkali- and volatile-rich primitive basalt responsible for Mount Etna's evolution in the last three decades. Earth and Planetary Science Letters 228, 1–17. https://doi.org/10.1016/j.epsl.2004.09.036

Métrich, N., Berry, A.J., O'Neill, H.S.C., Susini, J., 2009. The oxidation state of sulfur in synthetic and natural glasses determined by X-ray absorption spectroscopy. Geochimica et Cosmochimica Acta 73, 2382–2399. https://doi.org/10.1016/j.gca.2009.01.025

Mollo, S., Giacomoni, P.P., Coltorti, M., Ferlito, C., Iezzi, G., Scarlato, P., 2015. Reconstruction of magmatic variables governing recent Etnean eruptions: Constraints from mineral chemistry and P-T-fO_2-H_2O modeling. Lithos 212, 311–320. https://doi.org/10.1016/j.lithos.2014.11.020

Moore, L.R., Gazel, E., Tuohy, R., Lloyd, A.S., Esposito, R., Steele-MacInnis, M., Hauri, E.H., Wallace, P.J., Plank, T., Bodnar, R.J., 2015. Bubbles matter: An assessment of the contribution of vapor bubbles to melt inclusion volatile budgets. American Mineralogist 100, 806–823. https://doi.org/10.2138/am-2015-5036

Moretti, R., Baker, D.R., 2008. Modeling the interplay of fO_2 and fS_2 along the FeS-silicate melt equilibrium. Chemical Geology, 8th Silicate Melt Workshop 256, 286–298. https://doi.org/10.1016/j.chemgeo.2008.06.055

Moretti, R., Métrich, N., Arienzo, I., Di Renzo, V., Aiuppa, A., Allard, P., 2018. Degassing vs. eruptive styles at Mt. Etna volcano (Sicily, Italy). Part I: Volatile stocking, gas fluxing, and the shift from low-energy to highly explosive basaltic eruptions. Chemical Geology 482, 1–17. https://doi.org/10.1016/j.chemgeo.2017.09.017

Morizet, Y., Gennaro, E., Jego, S., Zajacz, Z., Iacono-Marziano, G., Pichavant, M., Carlo, I.D., Ferraina, C., Lesne, P., 2017. A Raman calibration for the quantification of SO_4^{2-}

groups dissolved in silicate glasses: Application to natural melt inclusions. American Mineralogist 102, 2065–2076. https://doi.org/10.2138/am-2017-6100

Moune, S., Holtz, F., Botcharnikov, R.E., 2009. Sulphur solubility in andesitic to basaltic melts: implications for Hekla volcano. Contributions to Mineralogy and Petrology 157, 691. https://doi.org/10.1007/s00410-008-0359-0

Moussallam, Y., Oppenheimer, C., Scaillet, B., Gaillard, F., Kyle, P., Peters, N., Hartley, M., Berlo, K., Donovan, A., 2014. Tracking the changing oxidation state of Erebus magmas, from mantle to surface, driven by magma ascent and degassing. Earth and Planetary Science Letters 393, 200–209. https://doi.org/10.1016/j.epsl.2014.02.055

Moussallam, Y., Edmonds, M., Scaillet, B., Peters, N., Gennaro, E., Sides, I., Oppenheimer, C., 2016. The impact of degassing on the oxidation state of basaltic magmas: A case study of Kīlauea volcano. Earth and Planetary Science Letters 450, 317–325. https://doi.org/10.1016/j.epsl.2016.06.031

Moussallam, Y., Longpré, M.-A., McCammon, C., Gomez-Ulla, A., Rose-Koga, E.F., Scaillet, B., Peters, N., Gennaro, E., Paris, R., Oppenheimer, C., 2019. Mantle plumes are oxidised. Earth and Planetary Science Letters 527, 115798. https://doi.org/10.1016/j.epsl.2019.115798

O'Neill, H.S.C., Berry, A.J., Mallmann, G., 2018. The oxidation state of iron in Mid-Ocean Ridge Basaltic (MORB) glasses: Implications for their petrogenesis and oxygen fugacities. Earth and Planetary Science Letters 504, 152–162. https://doi.org/10.1016/j.epsl.2018.10.002

Oppenheimer, C., 2003. Volcanic Degassing. Treatise on Geochemistry 3, 659. https://doi.org/10.1016/B0-08-043751-6/03020-6

Parkinson, I., Arculus, R.J., 1999. Redox state of subduction zones: insights from arc-peridotites. Chemical Geology 160, 408–423.

Pichavant, M., Scaillet, B., Di Carlo, I., Rotolo, S., Métrich, N., 2006. Sulfur in hydrous, oxidized basaltic magmas: phase equilibria and melt solubilities. Presented at the American Geophysical Union (AGU) 2006 joint assembly, EOS Trans. AGU, pp. 1–2.

Pichavant, M., Scaillet, B., Pommier, A., Iacono-Marziano, G., Cioni, R., 2014. Nature and Evolution of Primitive Vesuvius Magmas: an Experimental Study. Journal of Petrology 55, 2281–2310. https://doi.org/10.1093/petrology/egu057

Pownceby, M.I., O'Neill, H.S.C., 1994. Thermodynamic data from redox reactions at high temperatures. IV. Calibration of the Re-ReO_2 oxygen buffer from EMF and NiO+Ni-Pd redox sensor measurements. Contributions to Mineralogy and Petrology 118, 130–137. https://doi.org/10.1007/BF01052864

Richet, P., Whittington, A., Holtz, F., Behrens, H., Ohlhorst, S., Wilke, M., 2000. Water and the density of silicate glasses. Contributions to Mineralogy and Petrology 138, 337–347. https://doi.org/10.1007/s004100050567

Robidoux, P., Aiuppa, A., Rotolo, S.G., Rizzo, A.L., Hauri, E.H., Frezzotti, M.L., 2017. Volatile contents of mafic-to-intermediate magmas at San Cristóbal volcano in Nicaragua. Lithos 272, 147–163.

Robie, R.A., Hemingway, B.S., Fisher, J.R., 1979. Thermodynamic properties of minerals and related substances at 298.15 K and 1 bar (105 pascals) pressure and at higher temperatures (Report No. 1452), Bulletin.

Robock, A., 2000. Volcanic eruptions and climate. Reviews of Geophysics 38, 191–219. https://doi.org/10.1029/1998RG000054

Salem, L.C., Edmonds, M., Corsaro, R.A., Maclennan, J., 2019. Carbon dioxide in geochemically heterogeneous melt inclusions from Mount Etna, Italy Geochemistry, Geophysics, Geosystems. https://agupubs.onlinelibrary.wiley.com/doi/abs/10.1029/2018GC008027.

Salerno, G.G., Burton, M.R., Oppenheimer, C., Caltabiano, T., Randazzo, D., Bruno, N., Longo, V., 2009. Three-years of SO_2 flux measurements of Mt. Etna using an automated UV scanner array: Comparison with conventional traverses and uncertainties in flux retrieval. Journal of Volcanology and Geothermal Research 183, 76–83. https://doi.org/10.1016/j.jvolgeores.2009.02.013

Schiano, P., Clocchiatti, R., 1994. Worldwide occurrence of silica-rich melts in sub-continental and sub-oceanic mantle minerals. Nature 368, 621–624. https://doi.org/10.1038/368621a0

Schiavi, F., Rosciglione, A., Kitagawa, H., Kobayashi, K., Nakamura, E., Nuccio, P.M., Ottolini, L., Paonita, A., Vannucci, R., 2015. Geochemical heterogeneities in magma beneath Mount Etna recorded by 2001-2006 melt inclusions. Geochemistry, Geophysics, Geosystems 16, 2109–2126. https://doi.org/10.1002/2015GC005786

Shishkina, T.A., Botcharnikov, R.E., Holtz, F., Almeev, R.R., Portnyagin, M.V., 2010. Solubility of H_2O- and CO_2-bearing fluids in tholeiitic basalts at pressures up to 500MPa. Chemical Geology 277, 115–125. https://doi.org/10.1016/j.chemgeo.2010.07.014

Smith, P.M., Asimow, P.D., 2005. Adiabat_1ph: A new public front-end to the MELTS, pMELTS, and pHMELTS models. Geochemistry, Geophysics, Geosystems 6, Q02004. https://doi.org/10.1029/2004GC000816

Spilliaert, N., Allard, P., Métrich, N., Sobolev, A.V., 2006a. Melt inclusion record of the conditions of ascent, degassing, and extrusion of volatile-rich alkali basalt during the powerful 2002 flank eruption of Mount Etna (Italy). J Journal of Geophysical Research Solid Earth 111, B04203. https://doi.org/10.1029/2005JB003934

Spilliaert, N., Métrich, N., Allard, P., 2006b. S–Cl–F degassing pattern of water-rich alkali basalt: Modelling and relationship with eruption styles on Mount Etna volcano. Earth

and Planetary Science Letters 248, 772–786. https://doi.org/10.1016/j.epsl.2006.06.031

Stolper, E., 1982. Water in silicate glasses: An infrared spectroscopic study. Contributions to Mineralogy and Petrology 81, 1–17. https://doi.org/10.1007/BF00371154

Taylor, J.R., Wall, V.J., Pownceby, M.I., 1992. The calibration and application of accurate redox sensors. American Mineralogist 77, 284–295.

Thordarson, T., Self, S., 2003. Atmospheric and environmental effects of the 1783–1784 Laki eruption: A review and reassessment. Journal of Geophysical Research: Atmospheres 108, AAC 7-1-AAC 7-29. https://doi.org/10.1029/2001JD002042

Trigila, R., Spera, F.J., Aurisicchio, C., 1990. The 1983 Mount Etna eruption: thermochemical and dynamical inferences. Contributions to Mineralogy and Petrology 104, 594–608. https://doi.org/10.1007/BF00306667

Viccaro, M., Giacomoni, P.P., Ferlito, C., Cristofolini, R., 2010. Dynamics of magma supply at Mt. Etna volcano (Southern Italy) as revealed by textural and compositional features of plagioclase phenocrysts. Lithos 116, 77–91. https://doi.org/10.1016/j.lithos.2009.12.012

Von Aulock F.W., Kennedy B.M., Schipper C.I., Castro J.M., Martin D.E., Oze C., Watkins J.M., Wallace P.J., Puskar L., Bégué F., Nichols A.R.L. and Tuffen H., 2014. Advances in Fourier transform infrared spectroscopy of natural glasses: From sample preparation to data analysis. Lithos 206-207, 52-64.

Vidal, C.M., Métrich, N., Komorowski, J.-C., Pratomo, I., Michel, A., Kartadinata, N., Robert, V., Lavigne, F., 2016. The 1257 Samalas eruption (Lombok, Indonesia): the single greatest stratospheric gas release of the Common Era. Scientific Reports 6, 34868. https://doi.org/10.1038/srep34868

Wallace, P.J., Carmichael, I.S.E., 1994. S speciation in submarine basaltic glasses as determined by measurements of SKα X-ray wavelength shifts. American Mineralogist 79, 161–167.

Wallace, P.J., Edmonds, M., 2011. The Sulfur Budget in Magmas: Evidence from Melt Inclusions, Submarine Glasses, and Volcanic Gas Emissions. Reviews in Mineralogy and Geochemistry 73, 215–246. https://doi.org/10.2138/rmg.2011.73.8

Wallace, P.J., Plank, T., Edmonds, M., Hauri, E.H., 2015. Chapter 7 - Volatiles in Magmas, in: Sigurdsson, H. (Ed.), The Encyclopedia of Volcanoes (Second Edition). Academic Press, Amsterdam, pp. 163–183.

Waters, L.E., Lange, R.A., 2016. No effect of H_2O degassing on the oxidation state of magmatic liquids. Earth Planetary Science Letters 447, 48–59. https://doi.org/10.1016/j.epsl.2016.04.030

Webster, J.D., Botcharnikov, R.E., 2011. Distribution of Sulfur Between Melt and Fluid in S-O-H-C-Cl-Bearing Magmatic Systems at Shallow Crustal Pressures and Temperatures. Reviews in Mineralogy and Geochemistry 73, 247–283. https://doi.org/10.2138/rmg.2011.73.9

Wilke, M., Behrens, H., Burkhard, D.J.M., Rossano, S., 2002. The oxidation state of iron in silicic melt at 500 MPa water pressure. Chemical Geology 189, 55–67. https://doi.org/10.1016/S0009-2541 (02)00042-6

Zajacz, Z., Candela, P.A., Piccoli, P.M., Sanchez-Valle, C., 2012. The partitioning of sulfur and chlorine between andesite melts and magmatic volatiles and the exchange coefficients of major cations. Geochimica et Cosmochimica Acta 89, 81–101. https://doi.org/10.1016/j.gca.2012.04.039

Zajacz, Z., Candela, P.A., Piccoli, P.M., Sanchez-Valle, C., Wälle, M., 2013. Solubility and partitioning behavior of Au, Cu, Ag and reduced S in magmas. Geochimica et Cosmochimica Acta 112, 288–304. https://doi.org/10.1016/j.gca.2013.02.026

Zhang, H.L., Cottrell, E., Solheid, P.A., Kelley, K.A., Hirschmann, M.M., 2018. Determination of Fe3+/ΣFe of XANES basaltic glass standards by Mössbauer spectroscopy and its application to the oxidation state of iron in MORB. Chemical Geology 479, 166–175. https://doi.org/10.1016/j.chemgeo.2018.01.006

FIGURE CAPTIONS

Figure 1 - Backscattered electron images of experimental products: a) gas bubbles located at the glass/Pt-capsule interface (SPA2703#3); b) glass (SPA2704#4) with small sulphide globules; c)-d) internal walls of Pt-capsules showing reaction rims (Pt-Fe-S).

Figure 2 – S content of experimental glasses as function of a) oxygen fugacity (reported in bar and expressed as ΔNNO, i.e. log unit deviation from logfO_2 of the Nickel-Nickel Oxide oxygen buffer reaction), b) glass FeO_{tot} content, c) glass H_2O content and d) glass CO_2 content. FeO_{tot} concentrations are normalized on a volatile-free basis. The error bars indicate the standard deviation (1σ). "btw" = between.

Figure 3 – $DS^{fluid/melt}$ (calculated wt% S in fluid phase/ wt% S in basaltic melt) determined in this study, together with literature data (Beermann et al., 2015; Fiege et al., 2015; Le Gall, 2015; Lesne et al., 2011b; Zajacz et al., 2013). The data used to calibrate the empirical model described in the text are labelled "for model", while those that were not used are labelled "others". Decompression and annealing experimental data of Fiege et al. (2015) not used in the model are also shown in the plot. In the plot, the coloured curves show the dependence of $DS^{fluid/melt}$ on fO_2 predicted by the model *[1]* at variable T-P conditions.

Figure 4 - $Fe^{3+}/\Sigma Fe$ ratios determined by XANES spectroscopy available for some experimental glasses, plotted against $Fe^{3+}/\Sigma Fe$ ratios calculated from experimental fO_2 using equation *[2]* (Kress and Carmichael, 1991). Precisions (1σ) of XANES measurements are 0.013. Uncertainties on experimental $Fe^{3+}/\Sigma Fe$ ratios (between 0.010 and 0.052) are propagated from uncertainties on experimental fO_2 (see main text).

Figure 5 – a) FS olivine crystal entrapping a bubble-bearing MI. b) MI from FS tephra with typical scalloped edges. c) Typical MI with circular shape in 2013 olivine. d) Embayment surrounding the 2006-7 olivine crystal.

Figure 6 – $Fe^{3+}/\Sigma Fe$ ratios determined by XANES spectroscopy for Etnean MIs, the embayment (emb) and the matrix glass, as a function of a) CaO/Al_2O_3 ratios, b) MgO, c) K_2O, d) Na_2O, e) SiO_2, and f) FeO_{tot} contents in glass. The error bars indicate the standard deviation (1σ). The two black curves indicate the liquid lines of descend calculated by MELTS code (Ghiorso and Sack, 1995; Smith and Asimow, 2005) during fractional crystallization of ol+Mg-Cr-spinel → Fe-spinel + cpx+plg (plg only at the advanced step of fractional crystallization). See main text for details on this modelling. The two curves illustrate the simulations performed using a dP/dT = 3 MPa $°C^{-1}$, and an initial fO_2 of NNO+1 (dashed line) or NNO+2 (continuous line).

Figure 7 – $Fe^{3+}/\Sigma Fe$ ratios determined by XANES spectroscopy for MIs, one embayment in 2006-7 olivine and one matrix glass for 2002 sample versus their relative a) H_2O, b) S, c) CO_2 and d) Cl contents. Degassing curves for H_2O (a) and S (b) are modelled using the approach of Gaillard and Scaillet (2009) and Gaillard et al. (2011). The initial conditions of the simulations are given in the text and reported in Table S3 (in Supplementary Data Electronic Appendix_2).

Figure 8 – $Fe^{3+}/\Sigma Fe$ ratios determined by XANES spectroscopy for Etnean MIs and the embayment (emb) of 2006-7 olivine as a function of pressure (Table 4, this study and Gennaro et al., 2019), estimated from H_2O and CO_2 concentrations using the Iacono-Marziano et al. (2012) fluid-melt saturation model.

Figure 9 – a) Estimates of oxygen fugacity (expressed as ΔNNO, as defined in the caption of Figure 2 and in the main text) for the studied eruptions of Mt. Etna from $Fe^{3+}/\Sigma Fe$ ratios obtained by XANES. b) Estimates of oxygen fugacity for Mt. Etna from previous studies: S speciation (Métrich and Clocchiatti, 1996; Métrich et al., 2009; Morizet et al., 2017), experimental phase equilibria (Armienti et al., 1994; Métrich and Rutherford, 1998; Trigila et

al., 1991), olivine-spinel equilibria (Kahl et al., 2011; Kamenetsky and Clocchiatti, 1996). c) Comparison of fO_2 estimates from XANES data to those from the oxybarometer methods oxybarometer methods of Ballhaus et al. (1990, 1991) and Arató and Audétat (2017).

Figure 10 – S content versus a) MgO and b) K_2O contents of the MIs (data from this study and Gennaro et al., 2019). The two coloured curves indicate S contents calculated coupling equations *[6-7]* to the MELTS simulations with dP/dT = 3 and 20 MPa $°C^{-1}$ and initial fO_2 of NNO+2 (during fractional crystallization of ol+Mg-Cr-spinel→Fe-spinel + cpx+plg). Contoured symbols indicate data from Gennaro et al. (2019) for which fO_2 values have been estimated using olivine-spinel equilibrium (in yellow), spinel-melt equilibrium (in orange), or XANES $Fe^{3+}/\Sigma Fe$ ratios (in green).

Figure 11 – S content of melt inclusions (together with embayment of 2006 and matrix glass of 2002 samples) versus oxygen fugacity (expressed as ΔNNO, as defined in the caption of Figure 2 and in the main text), estimated from the XANES $Fe^{3+}/\Sigma Fe$ ratios and from oxybarometer methods of Arató and Audétat (2017) and Ballhaus et al. (1990, 1991). Also shown the behaviour of S as a function of fO_2 variation, upon the liquid lines of descent modelled by MELTS code coupled to the equations *[6-7]*.

Table 1 - Chemical composition of Mt. Spagnolo anhydrous starting glass.

oxide	wt %	±*
SiO_2	48.91	0.38
TiO_2	1.44	0.13
Al_2O_3	14.09	0.39
FeO	9.30	0.40
MnO	0.17	0.10
MgO	9.29	0.57
CaO	11.61	0.15
Na_2O	3.36	0.20
K_2O	1.27	0.10
P_2O_5	0.60	0.13
tot.	100.03	0.67

Oxides composition obtained by electron microprobe (EMP) analysis.

* = Standard deviation (1σ) calculated from 149 analysed points on two chips of the starting glass prepared in the same way (see main text for details) on two different days.

"FeO" is the total iron as FeO; "tot." is the total sum

Table 2 - Experimental conditions, starting and products phases, and oxygen fugacity (log fO_2) values estimated using both the experimental sensors and the $Fe^{3+}/\Sigma Fe$ ratios evaluated by XANES.

exp. number	wt% FeO added	wt% S added	XH_2O	wt% H_2O added	wt% CO_2 added	experimental					XANES 2018			
						*log fO_2	ΔNNO	±	$Fe^{3+}/\sum Fe$	±	$Fe^{3+}/\sum Fe$	±	log fO_2	ΔNNO
SPA1702: T=1200±5 °C P=1802±20 bars, time = 3 h; XCo = 0.22														
SPA1702#1	0.00	0.90	1.00	9.95	-	-7.15	0.6	0.1	**0.255**	0.011	n.d.	-	n.d.	n.d.
SPA1702#2	1.79	0.89	1.00	10.53	-	-7.16	0.6	0.1	**0.252**	0.011	n.d.	-	n.d.	n.d.
SPA1702#3	2.69	0.90	1.00	10.33	-	-7.12	0.7	0.1	**0.254**	0.011	**0.233**	0.013	7.37	0.3
SPA1702#5	1.78	0.90	0.74	5.77	5.04	-7.45	0.3	0.1	**0.231**	0.011	**0.226**	0.013	-7.52	0.3
SPA2703: T=1200±5 °C P=2100±20 bars, time = 3 h; XCo = 0.19														
SPA2703#1	3.56	1.78	1.00	11.09	-	-6.76	1.0	0.1	**0.284**	0.013	**0.222**	0.013	-7.45	0.3
SPA2703#2	3.62	3.62	1.00	9.55	-	-6.81	0.9	0.1	**0.283**	0.013	**0.275**	0.013	-6.91	0.8
SPA2703#3	3.57	1.80	0.77	5.91	4.45	-7.17	0.5	0.1	**0.247**	0.012	n.d.	-	n.d.	n.d.
SPA2703#4	3.57	3.60	0.77	6.00	4.38	-7.13	0.6	0.1	**0.253**	0.012	n.d.	-	n.d.	n.d.
SPA2704: T=1200±5 °C P=1930±20 bars, time = 3 h; XCo = 0.23														
SPA2704#1	4.52	1.78	1.00	9.63	-	-7.13	0.6	0.1	**0.255**	0.011	n.d.	-	n.d.	n.d.
SPA2704#2	5.46	1.79	1.00	8.92	-	-7.12	0.6	0.1	**0.250**	0.011	**0.221**	0.013	7.47	0.2
SPA2704#3	4.54	3.50	1.00	9.24	-	-7.15	0.6	0.1	**0.252**	0.011	n.d.	-	n.d.	n.d.
SPA2704#4	4.43	3.63	0.73	5.75	5.22	-7.51	0.2	0.1	**0.228**	0.010	**0.249**	0.013	-7.25	0.5
SPA2704: T=1200±5 °C P=2003±20 bars, time = 2 h; XCo = 0.12														
SPA1902#1	3.55	1.78	1.00	11.18	-	-5.98	1.7	0.5	**0.357**	0.052	n.d.	-	n.d.	n.d.
SPA1902#2	3.55	3.55	1.00	11.31	-	-5.98	1.7	0.5	**0.359**	0.051	n.d.	-	n.d.	n.d.

X_{H_2O} is the molar fraction of H_2O loaded in the initial fluid phase (X_{H_2O} = (mol. H_2O)/(mol. H_2O + mol. CO_2) = 1- X_{CO_2}). Logf_{O_2} (in bars) expressed as ΔNNO (the log deviation from logf_{O_2} of the Nickel-Nickel Oxide oxygen buffer reaction).

* Experimental logf_{O_2} values are calculated from the X_{Co} of the "sensor" method as described in the main text. The X_{CO} is calculated for each series of experimental run, and those reported in the table are average values (the standard deviation is 0.03 for about 15 analysis of each CoPd alloy, and has been neglected for the followed fO_2 calculation).

The relative $Fe^{3+}/\Sigma Fe$ ratio values are calculated using the Kress and Carmichael (1991) method *[2]*.

Using an inverse approach, the $Fe^{3+}/\Sigma Fe$ ratio, obtained from XANES methods, have been elaborated to obtain the relative logf_{O_2}.

All experimental products present a Fe-Pt-S reaction rim in the internal capsule wall.

n.d. = not determined

Table 3 - Major element composition and volatile contents of the experimental glasses, and S fluid/melt partition coefficients.

Exp. Number [#]	SiO_2	TiO_2	Al_2O_3	FeO_{tot} [°]	MnO	MgO	CaO	Na_2O	K_2O	P_2O_5	tot.[*]	Fe loss %	S_{melt} (ppm)	H_2O	CO_2	S_{fluid} (wt%)	$DS^{fluid/melt}$
SPA1702#1 *[15]*	50.59 (±0.47)	1.49 (±0.10)	14.61 (±0.22)	6.78 (±0.29)	0.16 (±0.08)	9.31 (±0.13)	11.81 (±0.15)	3.38 (±0.09)	1.30 (±0.08)	0.57 (±0.12)	94	-27 (±3)	858 (±88)	4.38 (±0.10)		12.3 (±3.5)	143 (±4)
SPA1702#2 *[30]*	50.80 (±0.31)	1.50 (±0.12)	14.65 (±0.19)	7.10 (±0.35)	0.18 (±0.10)	9.02 (±0.12)	11.72 (±0.13)	1.28 (±0.07)	3.25 (±0.08)	0.50 (±0.13)	93	-24 (±4)	925 (±112)	4.35 (±0.04)		11.1 (±3.0)	120 (±3)
SPA1702#3 *[30]*	49.90 (±0.40)	1.44 (±0.12)	14.31 (±0.17)	8.34 (±0.53)	0.15 (±0.08)	9.07 (±0.09)	11.58 (±0.12)	3.35 (±0.07)	1.30 (±0.07)	0.57 (±0.11)	94	-10 (±6)	1212 (±136)	4.42 (±0.03)		11.2 (±3.4)	92 (±4)
SPA1702#5 *[15]*	51.88 (±0.38)	1.55 (±0.11)	14.61 (±0.22)	5.88 (±0.24)	0.17 (±0.09)	8.89 (±0.06)	12.02 (±0.08)	1.32 (±0.08)	3.20 (±0.08)	0.48 (±0.13)	94	-37 (±3)	711 (±84)	3.27 (±0.04)	873 (±27)	10.3 (±6.3)	146 (±6)
SPA2703#1 *[95]*	49.72 (±0.54)	1.48 (±0.12)	14.28 (±0.20)	8.44 (±0.37)	0.15 (±0.11)	9.14 (±0.11)	11.64 (±0.16)	3.26 (±0.10)	1.30 (±0.09)	0.61 (±0.11)	92	-9 (±4)	1966 (±156)	5.19 (±0.03)		20.2 (±3.3)	103 (±3)
SPA2703#2 *[45]*	50.57 (±0.41)	1.45 (±0.09)	14.52 (±0.21)	6.96 (±0.71)	0.14 (±0.07)	9.31 (±0.11)	11.85 (±0.11)	3.30 (±0.09)	1.30 (±0.09)	0.59 (±0.13)	93	-25 (±8)	2215 (±219)	4.92 (±0.14)		40.4 (±10.3)	182 (±10)[+]
SPA2703#3 *[110]*	49.73 (±0.55)	1.45 (±0.12)	14.67 (±0.35)	7.75 (±0.38)	0.17 (±0.09)	9.30 (±0.13)	11.68 (±0.20)	3.34 (±0.08)	1.31 (±0.07)	0.60 (±0.13)	94	-17 (±4)	1170 (±109)	3.46 (±0.03)	1618 (±14)	20.5 (±6.5)	175 (±7)[+]
SPA2703#4 *[115]*	50.12 (±0.90)	1.44 (±0.10)	14.52 (±0.30)	7.48 (±0.35)	0.18 (±0.09)	9.26 (±0.11)	11.77 (±0.24)	3.34 (±0.08)	1.31 (±0.08)	0.58 (±0.13)	93	-20 (±4)	1340 (±110)	3.56 (±0.03)	1277 (±16)	34.42 (±13.6)	257 (±14)[+]
SPA2704#1 *[39]*	50.17 (±0.47)	1.45 (±0.09)	14.54 (±0.25)	7.43 (±0.70)	0.15 (±0.09)	9.22 (±0.15)	11.72 (±0.15)	3.46 (±0.08)	1.26 (±0.08)	0.61 (±0.14)	94	-20 (±7)	1252 (±179)	4.71 (±0.03)		24.4 (±11.1)	195 (±116)[+]
SPA2704#2 *[45]*	48.99 (±0.45)	1.40 (±0.09)	14.07 (±0.20)	9.63 (±0.47)	0.16 (±0.07)	9.12 (±0.10)	11.33 (±0.14)	3.42 (±0.08)	1.27 (±0.09)	0.61 (±0.14)	93	4 (±5)	1537 (±194)	4.63 (±0.22)		26.8 (±6.9)	175 (±7)[+]
SPA2704#3 *[68]*	49.96 (±0.32)	1.46 (±0.12)	14.37 (±0.19)	7.83 (±0.40)	0.17 (±0.09)	9.26 (±0.09)	11.60 (±0.14)	3.47 (±0.08)	1.29 (±0.08)	0.58 (±0.14)	94	-16 (±4)	1269 (±142)	4.56 (±0.10)		40.9 (±11.5)	323 (±12)[+]
SPA2704#4 *[74]*	50.94 (±0.54)	1.49 (±0.10)	14.84 (±0.21)	5.90 (±0.33)	0.17 (±0.09)	9.48 (±0.14)	11.66 (±0.15)	3.63 (±0.20)	1.33 (±0.09)	0.57 (±0.14)	94	-37 (±3)	856 (±141)	3.30 (±0.02)	767 (±8)	32.1 (±15.0)	375 (±15)[+]
SPA1902#1 *[45]*	49.44 (±0.38)	1.41 (±0.13)	14.00 (±0.17)	10.08 (±0.41)	0.16 (±0.04)	9.08 (±0.11)	11.36 (±0.11)	3.22 (±0.10)	1.26 (±0.09)	n.d.	93	8 (±4)	3595 (±30)	4.96 (±0.08)		17.9 (±3.6)	50 (±4)
SPA1902#2 *[33]*	49.93 (±0.38)	1.41 (±0.13)	14.11 (±0.17)	9.40 (±0.41)	0.16 (±0.04)	9.07 (±0.11)	11.39 (±0.11)	3.26 (±0.10)	1.27 (±0.09)	n.d.	92	1 (±4)	6039 (±232)	4.97 (±0.10)		30.6 (±3.5)	51 (±4)

All oxides (expressed in wt%) and S_{melt} (ppm = µg/g) contents are from EMP analysis. H_2O (wt%) and CO_2 (ppm) are from SIMS analysis. Major element concentrations are normalized to 100% on a volatile-free basis. $DS^{fluid/melt}$ = S_{fluid} (wt%)/S_{melt} (wt%), where S in the fluid (S_{fluid}, wt%) is

calculated following the procedure of Beermann et al. (2015), as described in the main text. Fe loss calculated as $100*(FeO_{exp}–FeO_{start})/(FeO_{start})$ where FeO_{exp} and FeO_{start} are from this table (= FeO_{tot}) and Table 1, respectively, after normalization to 100% on volatile-free basis.

Numbers between brackets are the standard deviations (1σ).

[#] The number between square brackets (in the first column) indicate the number of EMP analyses. Standard deviations (1σ) for H_2O and CO_2 concentrations are calculated on 5 repeated analyses for each glass.

[°] FeO_{tot} is the total iron as FeO; *tot. is the total sum of major oxides as obtained by EMP before the normalization to 100 wt%.

[+] These $DS^{fluid/melt}$ values are neither used in the discussion, nor in the regression model decribed in the main text because they are probably significantly affected by the presence of sulphides globules (see main text and supplementary for details).

n.d. = not determined

Table 4 - Chemical composition and volatile (H_2O, CO_2, S, Cl) contents of Etnean melt inclusions, one embayment and one matrix glass.

sample	Fo mol %	SiO_2	TiO_2	Al_2O_3	FeO_{tot}	MnO	MgO	CaO	Na_2O	K_2O	Cr_2O_3	P_2O_5	tot.	PEC %	H_2O	CO_2 (ppm)	S (ppm)	Cl (ppm)	Mg#	V_b/V_{MI}	size (µm) MI max	P (MPa)	Depth (km)
FS-XS_8# *[4]*	90	48.5 (0.4)	1.1 (0.2)	11.4 (0.2)	9.5 (0.3)	0.2 (0.1)	10.9 (0.2)	14.8 (0.1)	2.0 (0.1)	1.0 (0.1)	b.d.l.	0.6 (0.2)	92	1.5	5.77 (±0.04) *[2]*	2652 (±171) *[2]*	2330 (±110)	1820 (±140)	74.8	0.04	128	266	10.3
FS-XS_15# *[4]*	90	50.6 (0.3)	1.2 (0.2)	11.7 (0.2)	8.3 (0.6)	0.1 (0.0)	9.9 (0.3)	13.0 (0.4)	2.3 (0.1)	1.8 (0.1)	0.1 (0.0)	0.9 (0.1)	95	3.3	1.93 (±0.05) *[3]*	900 (±17) *[3]*	235 (±77)	1570 (±80)	74.5	0.03	225	129	5.0
FS-XS_20# *[4]*	90	49.3 (1.0)	1.0 (0.1)	10.7 (0.5)	8.8 (0.3)	0.1 (0.0)	10.7 (0.2)	16.0 (0.3)	2.0 (0.2)	0.8 (0.0)	0.1 (0.0)	0.4 (0.2)	90	7.4	2.81 (±0.07) *[3]*	1526	2980 (±178)	2688 (±74)	77.2	0.04	62.5	161	6.2
FS-XS_22a# *[4]*	90	49.1 (0.3)	1.2 (0.1)	12.0 (0.4)	8.5 (0.3)	0.1 (0.1)	9.1 (0.4)	15.8 (0.2)	2.2 (0.1)	1.3 (0.2)	0.1 (0.0)	0.5 (0.0)	91	11.1	4.81 (±0.09) *[2]*	2786 (±289) *[3]*	3445 (±168)	2488 (±158)	73.1	0.05	96	272	10.5
FS-XS_22b# *[4]*	90	49.5 (0.6)	1.2 (0.1)	11.3 (0.9)	8.7 (0.7)	0.1 (0.0)	9.4 (1.0)	16.3 (0.3)	2.0 (0.2)	1.0 (0.2)	0.1 (0.0)	0.5 (0.2)	92	14.0	2.33 (±0.31) *[2]*	2033 (±131) *[3]*	2613 (±103)	1968 (±62)	74.2	0.04	48.5	203	7.8
FS-XS_26b# *[3]*	90	49.9 (0.5)	1.1 (0.0)	13.2 (0.2)	9.4 (0.4)	0.2 (0.1)	10.6 (0.0)	11.9 (0.2)	2.3 (0.1)	1.3 (0.1)	n.d.	0.2 (0.1)	95	8.3	2.86 (±0.05) *[3]*	b.d.l.	b.d.l.	b.d.l.	74.1	0.12	195	62^+	2.4
FS-XS_28a# *[3]*	91	49.7 (0.2)	1.0 (0.1)	10.8 (0.1)	8.8 (0.4)	0.2 (0.1)	10.9 (0.3)	15.4 (0.1)	1.8 (0.1)	0.9 (0.0)	0.1 (0.0)	0.4 (0.1)	92	0.8	2.48 (±0.11) *[2]*	2079 (±17) *[2]*	2690 (±96)	1963 (±97)	77.4	0.05	64	221	8.5
FS-XS_28b# *[3]*	91	49.4 (0.2)	1.0 (0.2)	10.9 (0.3)	8.8 (0.2)	0.1 (0.1)	10.9 (0.2)	15.8 (0.1)	1.8 (0.0)	0.8 (0.2)	0.1 (0.0)	0.4 (0.1)	92	1.6	2.92 (±0.05) *[2]*	1892	2490 (±151)	3123 (±121)	76.9	0.07	95	201	7.7
FS-XS_30# *[3]*	90	50.2 (0.2)	0.9 (0.2)	11.7 (0.5)	8.7 (0.3)	0.2 (0.0)	10.5 (0.6)	14.4 (0.2)	2.0 (0.1)	1.0 (0.1)	0.1 (0.0)	0.3 (0.1)	92	9.8	2.51 (±0.06) *(2)*	1106	2308 (±166)	1653 (±90)	76.0	0.06	84	157	6.1
FS-XS_35# *[3]*	90	51.3 (0.2)	1.0 (0.1)	12.0 (0.1)	7.9 (0.3)	0.1 (0.1)	8.6 (0.1)	15.8 (0.0)	2.1 (0.0)	1.0 (0.1)	b.d.l.	0.2 (0.1)	92	10.3	3.99 (±0.02) *(2)*	1632 (±61) *(2)*	2460 (±145)	1507 (±196)	74.3	0.07	75.5	231	8.9
FS-XS_41# *[4]*	90	49.7 (0.4)	0.9 (0.1)	11.3 (0.2)	9.1 (0.5)	0.2 (0.1)	10.1 (0.5)	15.2 (0.5)	1.9 (0.0)	1.3 (0.0)	b.d.l.	0.3 (0.1)	94	1.6	4.31 (±0.02) *[2]*	687 (±207) *[3]*	1798 (±296)	1165 (±147)	73.4	0.08	160	139	5.4
FS_00* *[6]*	90	51.7 (0.3)	0.9 (0.2)	11.1 (0.1)	8.9 (0.4)	0.1 (0.1)	9.8 (0.1)	14.3 (0.2)	2.1 (0.1)	0.9 (0.1)	0.1	b.d.l.	95	0.1	3.70 (±0.05) *[2]*	882 (±93) *(2)*	1100 (±179)	1633 (±151)	73.0	0.20	180	167	6.4
Spa_3n* *[3]*	82	48.9 (0.0)	1.6 (0.2)	16.9 (0.0)	9.5 (0.8)	0.2 (0.1)	5.7 (0.2)	9.9 (0.1)	4.5 (0.0)	2.0 (0.1)	b.d.l.	0.6 (0.1)	97	8.4	0.16 (±0.07) *[2]*	b.d.l.	1515 (±49)	2280 (±156)	62.4	0.16	90	6^+	0.2
2002_26* *[2]*	73	51.7 (0.9)	2.1	16.6 (0.4)	9.5 (0.3)	0.1 (0.1)	3.2 (0.1)	6.8 (0.2)	5.2 (0.2)	3.9 (0.2)	b.d.l.	0.9 (0.1)	95	0.0	0.36	b.d.l.	225	1560	43.2	0.04	130	7^+	0.3

														(±0.02) *[3]*		(±78)	(±184)					
2002_30* *(4)*	74	52.2 (2.1)	1.4 (0.2)	17.6 (0.5)	9.3 (0.6)	0.2 (0.1)	3.9 (0.1)	6.5 (0.1)	5.1 (0.1)	2.9 (0.1)	n.d.	1.0 (0.1)	96	0.0	1.06	b.d.l.	343	2018	49.1	0.00	44	27^{+}	1.0
2002_32 matrix gl* *[2]*	73	49.8 (0.2)	2.0 (0.3)	16.1 (0.2)	10.5 (0.4)	0.3 (0.0)	3.8 (0.0)	8.4 (0.1)	4.9 (0.6)	3.3 (0.1)	n.d.	1.0 (0.1)	95	-	b.d.l.	b.d.l.	b.d.l.	1330 (±93)	44.9	-	-	-	-
2006_4* *[2]*	71	51.4 (0.0)	1.7 (0.1)	16.3 (0.1)	10.6 (0.0)	0.1 (0.1)	3.8 (0.0)	8.1 (0.1)	4.8 (0.0)	2.4 (0.0)	n.d.	0.9	96	0.0	0.92 (±0.02) *[2]*	470	380 (±28)	2390 (±226)	46.2	-	100	64	2.5
2006_7emb* *[2]*	8	49.5 (0.0)	1.9 (0.1)	16.8 (0.3)	11.0 (0.4)	0.3 (0.0)	3.5 (0.1)	8.8 (0.0)	4.5 (0.2)	3.4 (0.0)	n.d.	0.2	97	0.0	0.36	b.d.l.	525 (±262)	2240(±240)	42.1	-	-	7^{+}	0.3
2008_1* *[9]*	75	50.1 (0.3)	2.1 (0.1)	17.3 (0.2)	9.1 (0.4)	0.2 (0.1)	3.5 (0.1)	8.9 (0.2)	4.8 (0.1)	2.9 (0.2)	n.d.	1.0	98	0.9	0.13	430 (±64) *[2]*	284 (±6)	b.d.l.	45.5	-	140	43	1.7
2008_6A* *[3]*	70	54.9 (0.8)	0.9 (0.1)	18.0 (0.1)	7.2 (0.6)	0.2 (0.1)	2.2 (0.0)	7.7 (0.2)	4.4 (0.1)	3.4 (0.2)	n.d.	1.1	100	3.7	b.d.l.	b.d.l.	153 (±216)	1869 (±76)	40.7	0.01	40	n.d.	n.d.
2013_30* *[2]*	72	50.8 (0.3)	1.5 (0.0)	19.2 (0.0)	7.1 (0.0)	0.2 (0.1)	2.4 (0.1)	8.6 (0.3)	6.1 (0.3)	3.2 (0.1)	n.d.	0.9 (0.1)	96	0.0	0.14	b.d.l.	310	2675	41.8	0.11	70	4^{+}	0.2
2013_33*	70	52.7	0.9	21.2	4.9	0.1	1.5	3.1	8.4	5.8	n.d.	1.4	99	0.5	0.08	b.d.l.	137	1867	40.8	0.04	116	2^{+}	0.1
2013_34* *[2]*	71	54.0 (0.2)	1.6 (0.1)	20.2 (0.2)	6.3 (0.0)	0.2 (0.1)	2.0 (0.0)	5.2 (0.1)	6.4 (0.1)	3.9	n.d.	0.2	96	1.9	0.13	b.d.l.	270 (±51)	3350 (±114)	41.9	-	48	4^{+}	0.2

All oxides (expressed in wt%) and Cl contents (ppm) are from EMP analysis. H_2O (wt%) and CO_2 (ppm) evaluated in this study are from FTIR, while S and Cl concentrations are from EMP. Major elements are normalized to 100% on volatile-free basis, and corrected for PEC (PEC% = estimated amount (wt%) of Post-Entrapment Crystallization). Volatiles are not corrected for PEC.

Fo (mol%) is the fosterite content of the host olivine. Mg# calculated as molar MgO/FeO+MgO ratio, with FeO as Fe^{2+}.

V_b/V_{MI} means the ratio between bubble (inside the MI) volume and MI volume.

[#] = data from this study; * = data are from Gennaro et al. (2019); [+] = pressure and relative depth (below crater level) are calculated using 50 ppm of CO_2, considering the estimated CO_2 detection limit of FTIR method (e.g. Cecchetti et al., 2002; Von Aulock et al., 2014).

The number between square brackets (in the first column) indicate the number of EMP analyses; the number between square brackets in the column of H_2O and CO_2 indicate the number of FTIR or SIMS analyses. Standard deviations (1σ) are given for each oxide in brackets.

"tot." is the total sum of major oxides as obtained by EMP before the normalization to 100 wt%. b.d.l. = below detection limit; n.d. = not determined.

Standard deviations are given as precise as the shown digits and values given by "+/- 0.0" represent values under 0.05 rounded down.

Table 5 – XANES $Fe^{3+}/\Sigma Fe$ ratios and estimated oxygen fugacity (fO_2) determined for Etnean MIs, one embayment of the 2006 eruption, and one matrix glass in the 2002 sample.

Sample name	Fo mol%	S (ppm)	±	$Fe^{3+}/\sum Fe$	±	log fO_2	ΔNNO	note
FS-XS_8	90	2330	110	0.306	0.013	-6.6	1.1	*2018*
FS-XS_15	90	235	77	0.274	0.013	-7.0	0.7	*2018*
FS-XS_20	90	2980	178	0.352	0.013	-6.3	1.4	*2018*
FS-XS_22a	90	3445	165	0.327	0.013	-6.5	1.2	*2018*
FS-XS_22b	90	2613	103	0.329	0.013	-6.6	1.2	*2018*
FS-XS_26b	90	b.d.l.	-	0.301	0.013	-6.6	1.1	*2018*
FS-XS_28a	91	2690	96	0.358	0.013	-6.2	1.6	*2018*
FS-XS_28b	91	2490	151	0.336	0.013	-6.4	1.3	*2018*
FS-XS_30	90	2308	166	0.321	0.013	-6.5	1.2	*2018*
FS-XS_35	90	2460	145	0.333	0.013	-6.5	1.2	*2018*
FS-XS_41	90	1798	296	0.287	0.013	-6.9	0.8	*2018*
FS_00*	90	1100	179	0.277	0.013	-7.0	0.7	*2018*
Spa_3n*	82	1515	49	0.328	0.004	-6.8	1.4	*2015*
2002_26*	73	225	78	0.200	0.004	-8.7	-0.3	*2015*
2002_30*	74	343	74	0.229	0.013	-8.1	-0.4	*2018*
2002_32 matrix gl*	73	b.d.l.	-	0.206	0.004	-9.3	-0.6	*2015*
2006_4*	70	380	28	0.248	0.004	-7.9	0.4	*2015*
2006_7emb[a]	81	525	262	0.212	0.004	-8.8	-0.2	*2015*
2008_1*	75.	284	6	0.168	0.004	-9.5	-0.8	*2015*
2008_6A*	69	153	216	0.209	0.004	-8.7	-0.2	*2015*
2013_30*	72	310	-	0.177	0.004	-9.5	-0.9	*2015*
2013_33*	70	137	51	0.225	0.013	-8.9	-0.4	*2018*
2013_34*	71	270	-	0.214	0.004	-8.8	-0.2	*2015*

$Fe^{3+/}\Sigma Fe$ ratios are obtained from XANES spectra acquired during 2015 and 2018 sessions (see main text and Supplementary Data Electronic Appendix_1 for details). The log fO_2 values are calculated from $Fe^{3+/}\Sigma Fe$ ratios using the empirical equation *[2]* of Kress and Carmichael (1991) in a temperature range of 1050-1200 °C and a pressure estimated from H_2O and CO_2 contents (see text for calculation details and Table 5). The error associated with

the calculated NNO value is between 0.1 and 0.2, depending on the error associated with the $Fe^{3+}/\Sigma Fe$ ratio (±0.004 to ±0.013).

*Fo (fosterite content of the host olivine) and S (ppm) data are from Gennaro et al. (2019).

emb= embayment, gl = glass.

b.d.l. = below detection limit

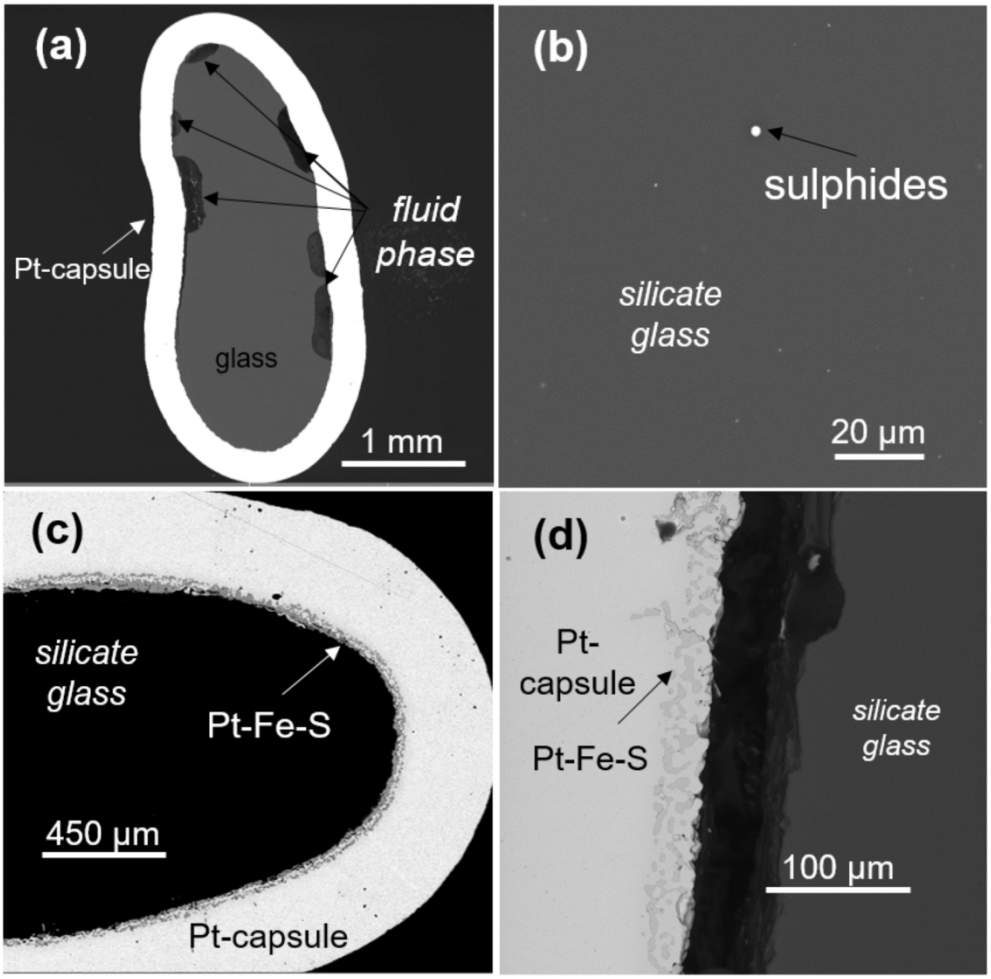

Figure 1 - Backscattered electron images of experimental products: a) gas bubbles located at the glass/Pt-capsule interface (SPA2703#3); b) glass (SPA2704#4) with small sulphide globules; c)-d) internal walls of Pt-capsules showing reaction rims (Pt-Fe-S).

152x148mm (300 x 300 DPI)

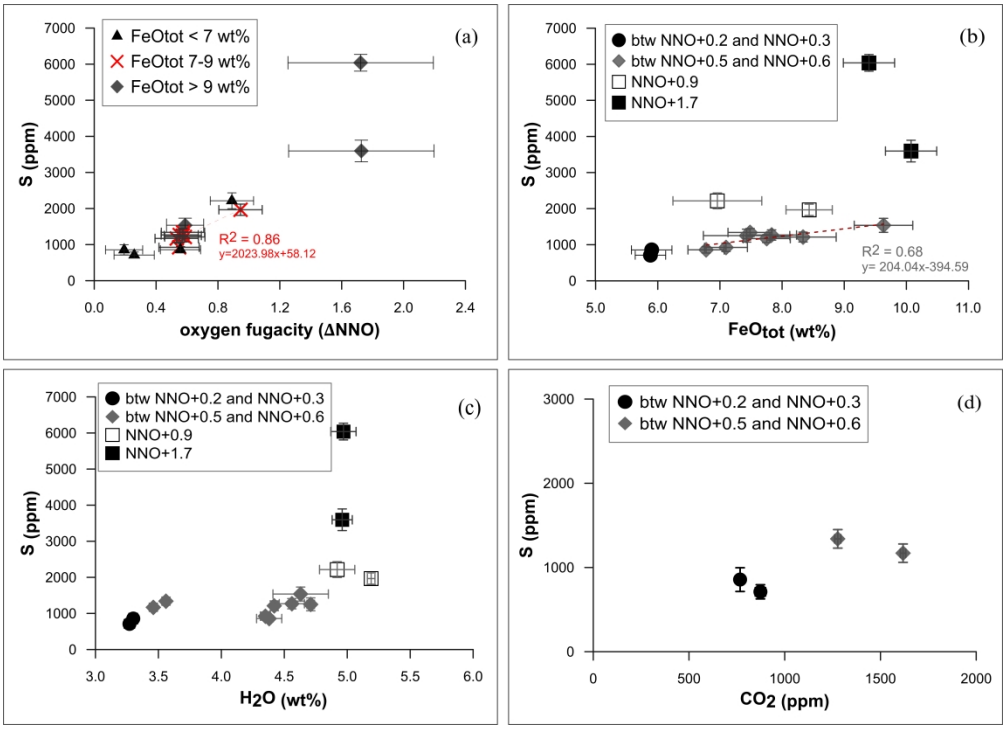

Figure 2 – S content of experimental glasses as function of a) oxygen fugacity (reported in bar and expressed as ΔNNO, i.e. log unit deviation from logfO2 of the Nickel-Nickel Oxide oxygen buffer reaction), b) glass FeOtot content, c) glass H2O content and d) glass CO2 content. FeOtot concentrations are normalized on a volatile-free basis. The error bars indicate the standard deviation (1σ). "btw" = between.

603x434mm (300 x 300 DPI)

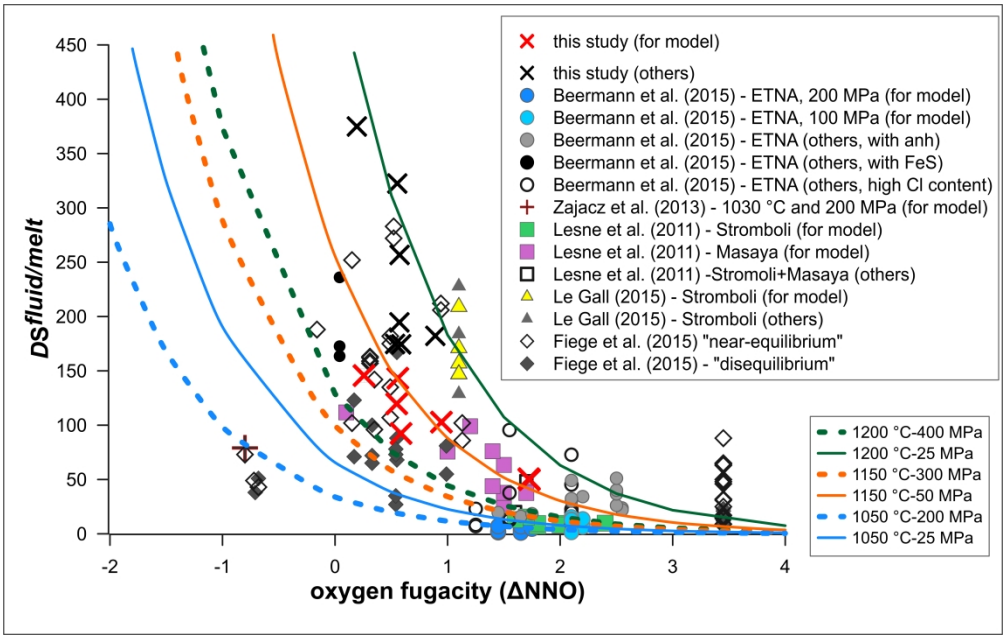

Figure 3 – DSfluid/melt (calculated wt% S in fluid phase/ wt% S in basaltic melt) determined in this study, together with literature data (Beermann et al., 2015; Fiege et al., 2015; Le Gall, 2015; Lesne et al., 2011b; Zajacz et al., 2013). The data used to calibrate the empirical model described in the text are labelled "for model", while those that were not used are labelled "others". Decompression and annealing experimental data of Fiege et al. (2015) not used in the model are also shown in the plot. In the plot, the coloured curves show the dependence of DSfluid/melt on fO2 predicted by the model [1] at variable T-P conditions.

471x297mm (300 x 300 DPI)

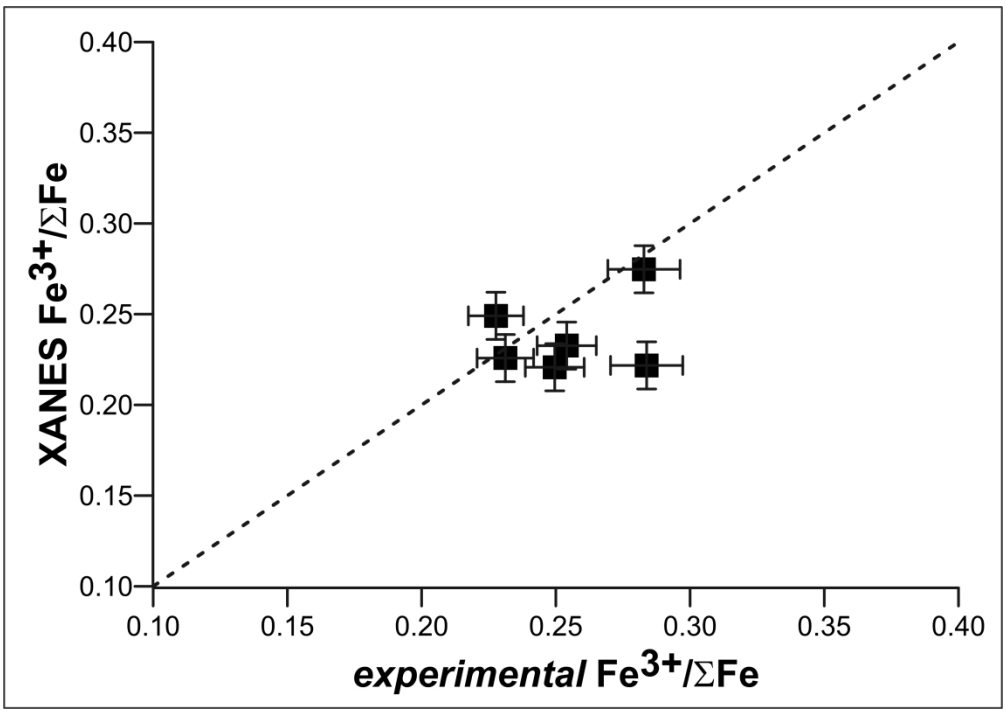

Figure 4 - Fe3+/ΣFe ratios determined by XANES spectroscopy available for some experimental glasses, plotted against Fe3+/ΣFe ratios calculated from experimental fO2 using equation [2] (Kress and Carmichael, 1991). Precisions (1σ) of XANES measurements are 0.013. Uncertainties on experimental Fe3+/ΣFe ratios (between 0.010 and 0.052) are propagated from uncertainties on experimental fO2 (see main text).

279x196mm (300 x 300 DPI)

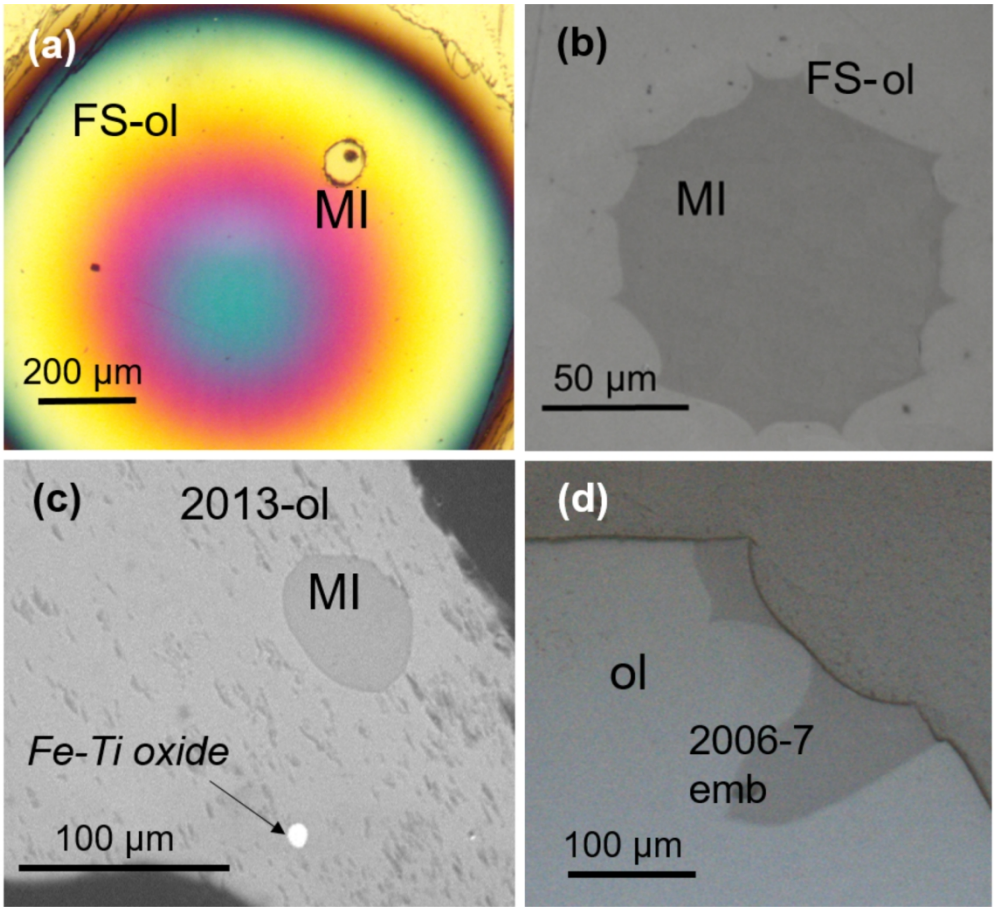

Figure 5 – a) FS olivine crystal entrapping a bubble-bearing MI. b) MI from FS tephra with typical scalloped edges. c) Typical MI with circular shape in 2013 olivine. d) Embayment surrounding the 2006-7 olivine crystal.

152x137mm (300 x 300 DPI)

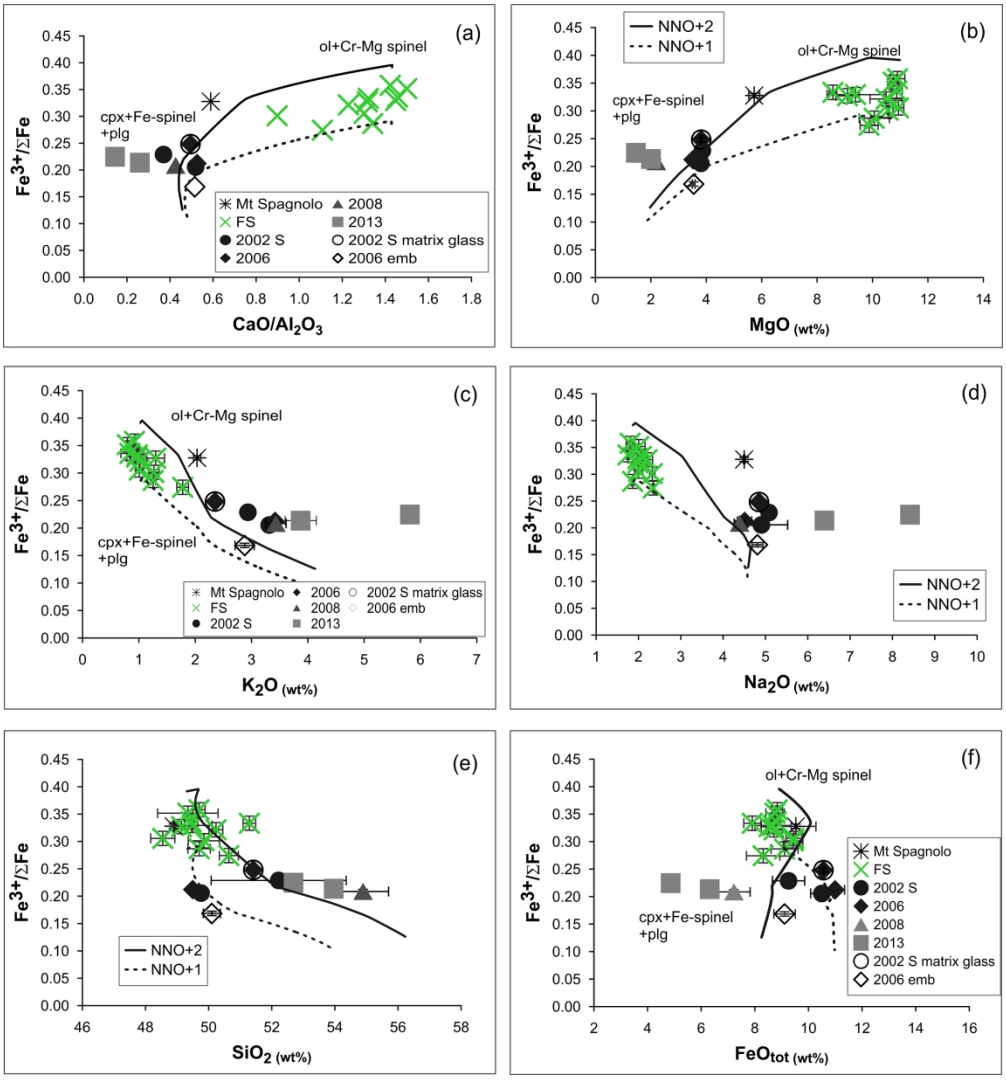

Figure 6 – Fe3+/ΣFe ratios determined by XANES spectroscopy for Etnean MIs, the embayment (emb) and the matrix glass, as a function of a) CaO/Al2O3 ratios, b) MgO, c) K2O, d) Na2O, e) SiO2, and f) FeOtot contents in glass. The error bars indicate the standard deviation (1σ). The two black curves indicate the liquid lines of descend calculated by MELTS code (Ghiorso and Sack, 1995; Smith and Asimow, 2005) during fractional crystallization of ol+Mg-Cr-spinel □ Fe-spinel + cpx+plg (plg only at the advanced step of fractional crystallization). See main text for details on this modelling. The two curves illustrate the simulations performed using a dP/dT = 3 MPa °C-1, and an initial fO2 of NNO+1 (dashed line) or NNO+2 (continuous line).

230x246mm (300 x 300 DPI)

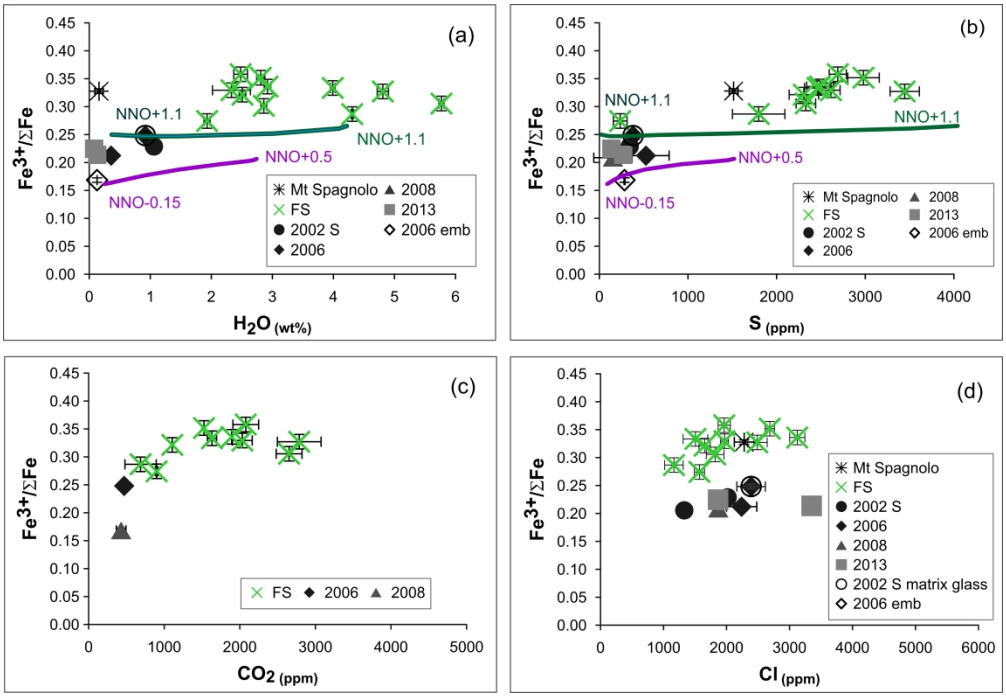

Figure 7 – Fe3+/ΣFe ratios determined by XANES spectroscopy for MIs, one embayment in 2006-7 olivine and one matrix glass for 2002 sample versus their relative a) H2O, b) S, c) CO2 and d) Cl contents. Degassing curves for H2O (a) and S (b) are modelled using the approach of Gaillard and Scaillet (2009) and Gaillard et al. (2011). The initial conditions of the simulations are given in the text and reported in Table S3 (in Supplementary Data Electronic Appendix_2).

552x381mm (300 x 300 DPI)

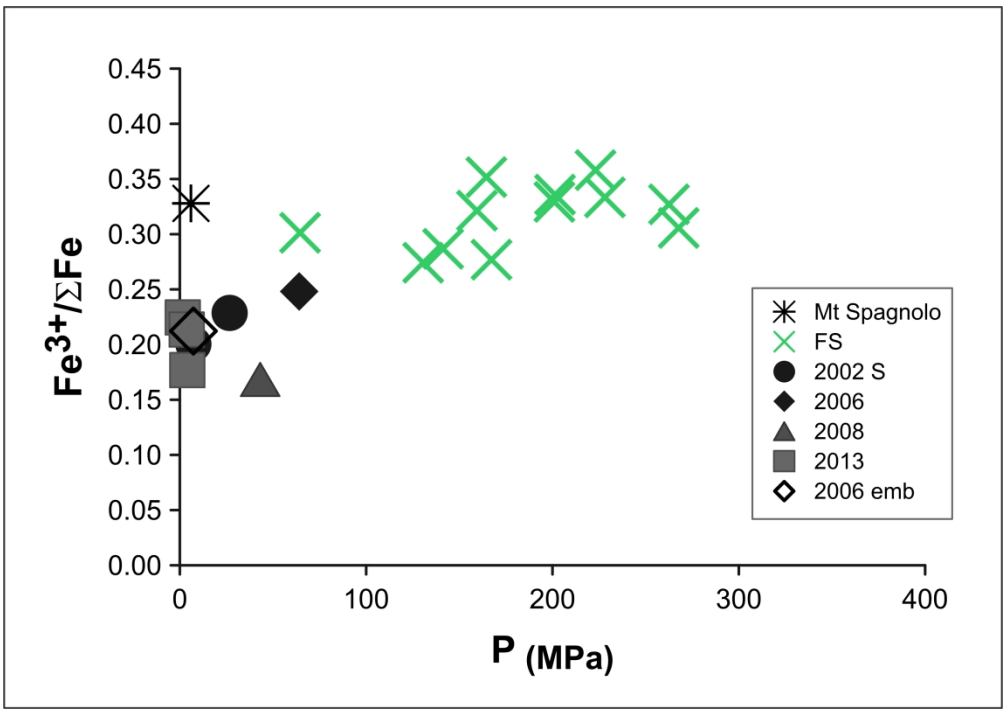

Figure 8 – Fe3+/ΣFe ratios determined by XANES spectroscopy for Etnean MIs and the embayment (emb) of 2006-7 olivine as a function of pressure (Table 4, this study and Gennaro et al., 2019), estimated from H2O and CO2 concentrations using the Iacono-Marziano et al. (2012) fluid-melt saturation model.

279x196mm (300 x 300 DPI)

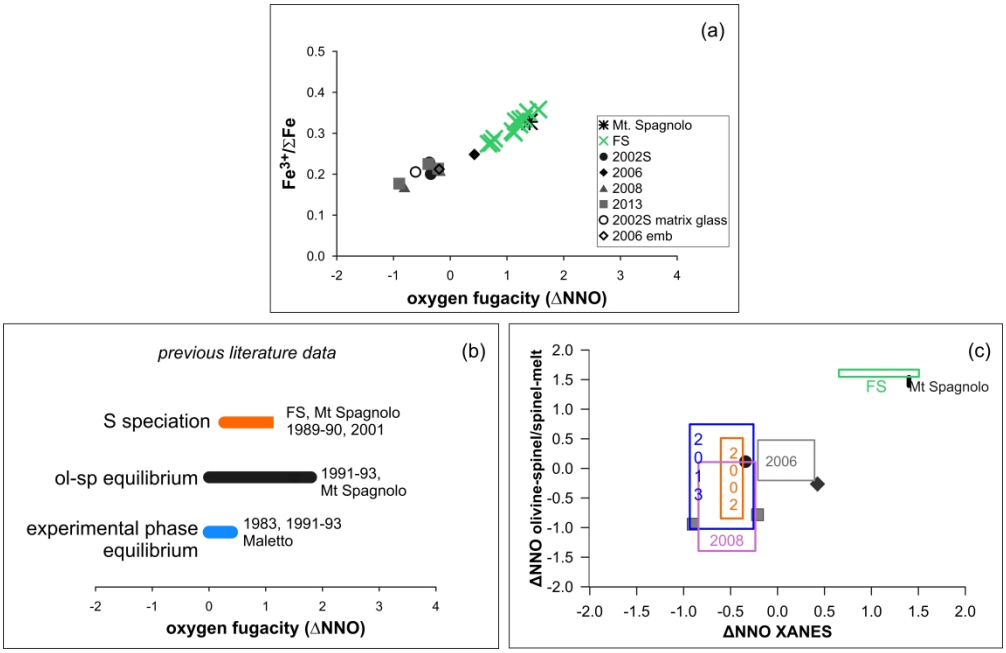

Figure 9 – a) Estimates of oxygen fugacity (expressed as ΔNNO, as defined in the caption of Figure 2 and in the main text) for the studied eruptions of Mt. Etna from Fe3+/ΣFe ratios obtained by XANES. b) Estimates of oxygen fugacity for Mt. Etna from previous studies: S speciation (Métrich and Clocchiatti, 1996; Métrich et al., 2009; Morizet et al., 2017), experimental phase equilibria (Armienti et al., 1994; Métrich and Rutherford, 1998; Trigila et al., 1991), olivine-spinel equilibria (Kahl et al., 2011; Kamenetsky and Clocchiatti, 1996). c) Comparison of fO2 estimates from XANES data to those from the oxybarometer methods oxybarometer methods of Ballhaus et al. (1990, 1991) and Arató and Audétat (2017).

644x415mm (300 x 300 DPI)

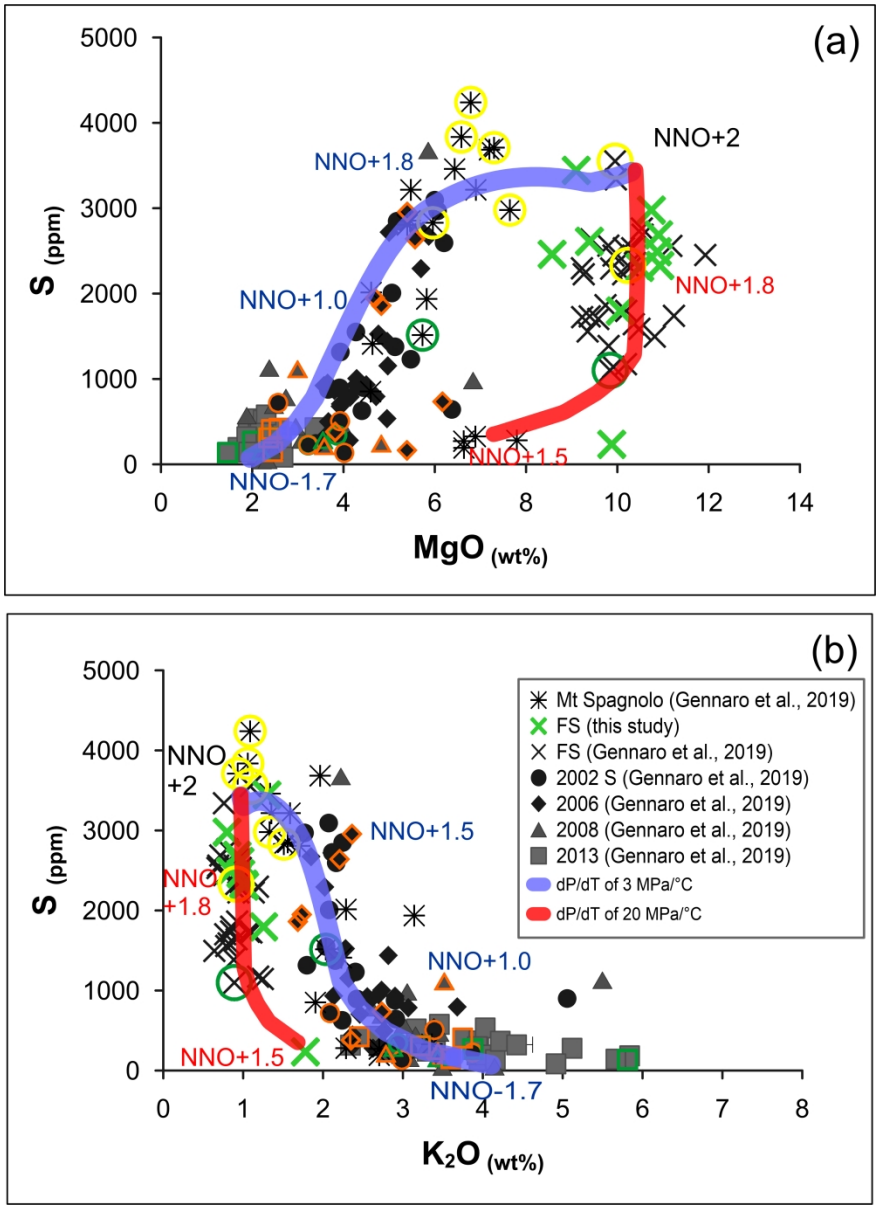

Figure 10 – S content versus a) MgO and b) K2O contents of the MIs (data from this study and Gennaro et al., 2019). The two coloured curves indicate S contents calculated coupling equations [6-7] to the MELTS simulations with dP/dT = 3 and 20 MPa °C-1 and initial fO2 of NNO+2 (during fractional crystallization of ol+Mg-Cr-spinel□Fe-spinel + cpx+plg).
Contoured symbols indicate data from Gennaro et al. (2019) for which fO2 values have been estimated using olivine-spinel equilibrium (in yellow), spinel-melt equilibrium (in orange), or XANES Fe3+/ΣFe ratios (in green).

284x391mm (300 x 300 DPI)

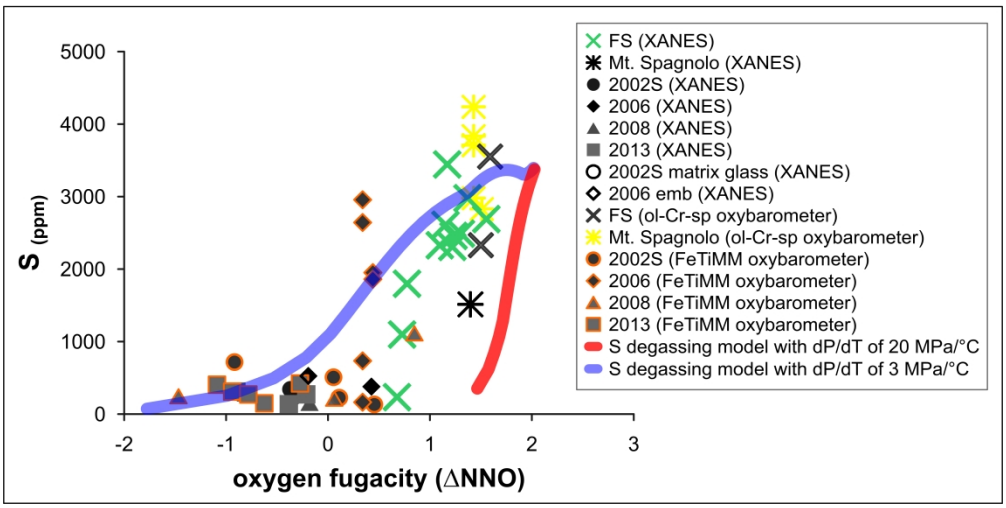

Figure 11 – S content of melt inclusions (together with embayment of 2006 and matrix glass of 2002 samples) versus oxygen fugacity (expressed as ΔNNO, as defined in the caption of Figure 2 and in the main text), estimated from the XANES Fe3+/ΣFe ratios and from oxybarometer methods of Arató and Audétat (2017) and Ballhaus et al. (1990, 1991). Also shown the behaviour of S as a function of fO2 variation, upon the liquid lines of descent modelled by MELTS code coupled to the equations [6-7].

413x217mm (300 x 300 DPI)